ATOMIC FORCE MICROSCOPY EXPERIMENTS ON ATOMICALLY THIN MATERIALS

A THESIS SUBMITTED TO

THE GRADUATE SCHOOL OF ENGINEERING AND SCIENCE

OF BILKENT UNIVERSITY

IN PARTIAL FULFILLMENT OF THE REQUIREMENTS FOR

THE DEGREE OF

MASTER OF SCIENCE

IN

PHYSICS

By

Ali Sheraz

24 June, 2020

Atomic Force Microscopy Experiments on Atomically Thin Materials
By Ali Sheraz
24 June, 2020

We certify that we have read this thesis and that in our opinion it is fully adequate, in scope and in quality, as a thesis for the degree of Master of Science.

Talip Serkan Kasırga(Advisor)

Onur Tokel

Cem Sevik

Approved for the Graduate School of Engineering and Science:

Ezhan Karaşan
Director of the Graduate School

ABSTRACT

ATOMIC FORCE MICROSCOPY EXPERIMENTS ON ATOMICALLY THIN MATERIALS

Ali Sheraz
M.Sc. in Physics
Advisor: Talip Serkan Kasırga
24 June, 2020

In 2004, successful isolation of graphene attracted immense attention of scientists because of atomic scale thickness and exotic functionalities. Regardless of graphene's thickness and extraordinary properties only reason that limits the usage of graphene in electronics is no band gap. But there is a way to open band gap of graphene by introducing defects or applying electric field but defects introduction can affect its functionality. So, world moved towards transition metal dichalcogenides (TMDCs), new analogs of graphene with thickness dependent band gap option are promising nominee for potential applications in modern physics and electronics. Besides electronic properties, TMDCs depict excellent mechanical characteristics (in plane elastic modulus, breaking strength/strain and pretension) compared to conventional volumetric counterparts.

The objective of this study is to investigate work function and mechanical properties of atomically thin materials using Kelvin probe force microscopy (KPFM) and Nanoindentation modes of Asylum Atomic Force Microscopy (AFM) respectively. Firstly, KPFM experiments were performed on CVD grown Vanadium Sesquioxide V_2O_3 to map surface potential variation and calculated work function value 4.91 eV. This will help in understanding band alignment, contact resistance and appropriate Schottky barrier height (SBH) by choosing metal contacts with closer work function to V_2O_3.

Secondly by using AFM based nanoindentation we first time reported elastic features of metallic TMDCs: 2H-TaS_2, 3R-NbS_2, 1T-$TaTe_2$ and 1T-$NbTe_2$ with various thickness values suspended over circular holes. Comprehensive measurement was done on 2H-TaS_2 and found thickness independent Young's modulus for 2H-TaS_2 is 114 $\pm$ 14 GPa, breaking strength 12.6 $\pm$ 2.6 GPa corresponds to nominal strain of 11% and ultimate strain of 0.22. Same mechanical features were

investigated for other three materials and they also manifested extreme elasticity and high strain values compare to other 2D materials reported so far except graphene.

This mechanical analysis of metallic materials will contribute in future flexible nano technological devices (for instance piezo electronics), wearable electronics, resistive coatings in electronic devices, nanoelectromechanical systems (NEMS) and strain sensors.

Keywords: Vanadium Sesquioxide, Transition Metal Dichalcogenides, Kelvin Probe Force Microscopy, Nanoindentation.

ÖZET

ATOMIK INCELIKTEKI MALZEMELERDE ATOMIK KUVVET MIKROSKOBU DENEYLERI

Ali Sheraz
Fizik, Yüksek Lisans
Tez Danışmanı: Talip Serkan Kasırga
24 June, 2020

2004'te, grafenin başarılı izolasyonu atomik ölçekteki kalınlığı ve egzotik fonksiyonalite nedeniyle bilim insanlarının dikkatini çekti. Grafenin kalınlığı ve sıra dışı özellikleri ne olursa olsun bu materyalin elektronik uygulamalarda kullanılamamasının tek nedeni bant genişliğinin olmamasıdır. Fakat, grafenin bant genişliği çeşitli kusurlar oluşturularak veya elektrik alan uygulayarak açılabilir ama bu kusurlar grafenin fonksiyonelliğini etkileyebilir. Bu nedenle dünya, grafenin yeni analoğu olan kalınlığa bağlı bant genişliği değişebilen ve modern fizik ve elektronik uygulamarına aday olan geçiş metali dikalkojenitleri (TMDC'lere) doğru yöneldi. Elektronik özelliklerinin yanında, bu TMDC'ler konvansiyonel hacimsel akranlarına kıyasla mükemmel mekanik özellikler (kırılma kuvveti, düzlemsel elastik modül, başlangıç gerginliği) gösteriyorlar.

Bu çalışmanın amacı atomik kalınlıktaki materyallerin mekanik özelliklerinin ve iş fonksiyonlarının Asylum Atomik Kuvvet Mikroskopunun (AKM) Kelvin Prob Kuvvet Mikroskobu (KPKM) ve nanoindentasyon modları ile araştırılmasıdır. İlk olarak, KPKM deneyleri CVD ile büyütülmüş Vanadyum Sesquioksit (V_2O_3) üstünde yüzey potansiyelini haritalandırmak için gerçekleştirildi ve iş fonksiyonlarının 4.91 eV olarak hesaplandı. Bu, bant hizalanmasının, kontak direncinin ve Schottky bariyer yüksekliğinin V_2O_3 iş fonksiyonuna yakın metal kontaklar seçilerek anlaşılmasına yardımcı olacak.

İkinci olarak, biz AKM tabanlı nanoindentasyon kullanarak ilk defa metalik TMDC'lerin (dairesel delikler üstünde askıda bırakılan çeşitli kalınlıklardaki 2H-TaS_2, 3R-NbS_2, 1T-$TaTe_2$ and 1T-$NbTe_2$) elastik özelliklerini raporladık. 2H-TaS_2 üstünde geniş çaplı ölçümler yapıldı ve kalınlıktan bağımsız Young modülü 114±14 GPa, kırılma kuvveti 12.6±2.6 GPa büyüklüğüne karşılık gelen 11% esneme değeri ve 0.22 nihai esneme bulundu. Aynı mekanik özellikler diğer üç

materyal için de araştırıldı ve onlar da grafen hariç 2D malzemelere kıyasla olağanüstü elastisite ve yüksek esneme değerleri gösterdiler.

Metalik malzemelerin mekanik açıdan analiz edilmesi, gelecekteki esnek nanoteknolojik aygıtların (piezoelektronik cihazlar gibi), giyilebilir elektronik cihazların, elektronik dirençli kaplamaların, nanoelektromekanik sistemlerin (NEMS) ve gerilim sensörleri gibi teknolojilerin gelişmesine katkıda bulunacaktır.

Anahtar sözcükler: Vanadyum Sesquioksit, Geçiş Metali Dikalkojenitler, Kelvin Prob Kuvvet Mikroskobu, Nanoindentasyon.

Acknowledgement

All glorification is because of ALLAH, most beneficent, merciful and king of the universe. I am very blessed and thankful to ALLAH who enabled me to complete my research work successfully. Then, I would like to express my sincere gratitude to my advisor Dr. Talip Serkan Kasırga for giving me research opportunity, immense encouragement, his faith in me during research and gracious support throughout my degree. I could not have imagined such a brilliant end of my master's research without his progressive guidance and excellent supervision.

I am thankful to my thesis jury members: Dr. Cem Sevik and Dr. Onur Tokel for generously offering their time, insightful comments and suggestions for my thesis. I would like to say thanks to Dr. Engin Durgun and his student Mert Miraç Çiçek for DFT calculations. Also, I owe some sincere gratitudes to Dr. Ceyhun Bulutay, Dr. Cemal Yalabik, Dr.Bülend Ortaç and Dr. Oğuz Gülseren for teaching me physics courses and excellent scientific discussions.

I gratefully acknowledge the guidance, help and contribution of my colleague Naveed Mehmood from the very first day of me in SCM Lab. I am thankful to Ibrahim for helping in data analysis and Turkish translation of thesis abstract, Hamid for scientific discussions and ideas and also thanks to Merve. Also, I am thankful to former SCM Lab members, especially Engin Can Surmeli and Onur Çakıroğlu for training me research equipments and tools.

It is a pleasure to mention my friends for their wonderful times and fun we made together. I am exceptionally grateful to my best friend Samar for everything (I don't have words to praise her, she supported me during my good and bad times a lot). Then, I am grateful to mention Misbah Bhabi and Salahuddin Bhai (for unlimited love, guidance, friendship, care and unlimited food invitations as well), Anjum Bhai and Faiza Bhabi (for delicious choul), Naveed Bhai and Breera Bhabi. Also, I am thankful to other friends Luqman Saleem (special thanks for help in academia), Farhan, Hilal, Naveed-ul-Mustafa, Talha Masood, Sabeeh, Amna, Mubashira, Aamir, Hamza Humayun, Ahsen and Ahmad for beautiful

times and friendship.

Finally yet importantly, I want to say special and sincere thanks to my beloved maternal mother Shaukat Bibi (Late) for raising me up from my childhood and made me what I am today and she must be feeling proud on my success and I dedicate this milestone to her. Also, gratitude goes to my maternal father (Malik Sab, I am forever indebted to you), my parents (Qaiser Abbas and Gulzar Qaiser) and my siblings for their endless respect, prayers, unparalleled love and encouragement that was worth more than I can write here. This journey would not have been possible without selfless love and encouragement of my family.

Contents

1 Introduction **1**

1.1 Brief Historical Introduction of Two Dimensional Materials 1

1.2 Thesis Goal 4

1.3 Atomic Force Microscope Details (AFM) 4

1.3.1 AFM Operational Modes 5

1.3.2 Dynamic Mode 7

1.4 Revealing Electrical and Nanomechanical Properties 8

1.4.1 Electrical Properties 8

1.4.2 Nanomechanical Properties 9

1.5 Outline 10

2 Extensive literature survey of KPFM and Nano-Indentation **12**

2.1 What is Work Function? 12

2.2 Measurement of Work Function: Experimental Techniques 14

2.2.1 Method of Diode 14

2.2.2 Kelvin Probe Method: Contact Potential Difference (CPD) 14

2.2.3 Work Function of Vanadium Sesquioxide ($\mathbf{V_2O_3}$) 20

2.3 Determination of Mechanical Properties of TMDCs 22

2.3.1 Young's Modulus 22

2.3.2 Metallic TMDCs ($\mathbf{MX_2 : M = Ta, Nb - X = S, Te}$) . . . 24

2.3.3 Metallic TMDCs Mechanical Properties Measurement Method 25

2.3.4 Analysis of F-D curves using Continuum Mechanics Model 28

3 Experimental Protocols 34

3.1 Instrumental description 34

3.2 Experimentation for KPFM 35

3.2.1 AFM Probes for KPFM 35

3.2.2 Sample Preparation for KPFM Measurements 36

3.3 Mapping of Surface Contact Potential Difference (CPD) using KPFM 37

3.4 Sample Preparation for Nanoindentation 40

3.4.1 Cleaned Holey Substrate Preparation via Focused Ion Beam (FIB) 40

3.4.2 Isolation or Fabrication of Ultrathin TMDCs 41

3.5 Calibration of AFM Probes and Deflection Sensitivity 45

3.5.1 AFM Probes 45

3.5.2 Calibration of AFM Probe's Spring Constant 46

3.6 AFM Imaging and Nanoindentation 49

3.6.1 AFM Tip-Sample Interaction Steps 50

3.6.2 Nanoindentation 51

4 Results and Discussion 54

4.1 Identification/Characterization of ultrathin flakes 55

4.1.1 Optical Microscopy 55

4.1.2 Raman Spectroscopy 56

4.2 Atomic Force Microscopy (AFM) Experiments 59

4.2.1 Measurement of Work Function of $\mathbf{V_2O_3}$ using KPFM . . 60

4.2.2 Measurement of Mechanical Properties of Various Ultrathin 2D Materials via F-D Curves 63

5 Conclusion and Future Work 78

List of Figures

1.1 Position of transition metals along with chalcogenides in periodic table 3

1.2 AFM schematic setup 5

1.3 (a) AFM Static mode working principle (b) tip follows contour path (c) tip scans sample in raster pattern 6

1.4 AFM Dynamic mode working principle 7

1.5 AFM Force-distance curve depicting various interaction regions . 10

2.1 Band alignment comparison of two metals 13

2.2 Mechanism of KPFM. (a) two metals having different values of work functions come into contact (b) Fermi level alignments (electron flow from less work function metal to higher untill CPD generates because of build in electric field) (c) external potential needed to nullify CPD (re-alignment of Fermi levels) 16

2.3 First trace for topography 18

2.4 Second trace lifting of tip to detect electrostatic forces at surface . 18

2.5 V_2O_3 Pressure-temperature picture 21

2.6 Stress-strain relationship diagram consisting of two regions 23

2.7 2H-TaS_2 Crystal structure (a) top (b) side view 24

2.8 (A) SEM image of suspended graphene over holes (B) Non-contact mode topographical image of graphene flake over hole (C) Schematic setup for nanoindentation (D) Fractured topographical image after maximum indentation 26

2.9 Force-deflection curves for monolayer and bilayer MoS_2 27

2.10 AFM based nanoindentation schematic 27

2.11 Loading curve showing linear and cubic regimes under different forces 30

2.12 FD Curves for mica showing non-linear behave for 2-6 layer while 12 layers showing linear trend under applied load 31

2.13 AFM nanoindentation block diagram 33

3.1 Asylum AFM setup at UNAM 35

3.2 SEM images of KPFM probes 36

3.3 Schematic of Asylum KPFM setup 38

3.4 Sketch map for KPFM scanning process 39

3.5 FIB drilled holes SEM images 41

3.6 NbS_2 CVD growth setup 42

3.7 Optical images of 2H-TaS_2 exfoliated flakes on PDMS stamp (Scale bar is 10 μm) 43

3.8 (a) Deterministic dry transfer method setup (b) procedure using PDMS viscoelastic stamp, inset shows SCM Lab dry transfer setup 44

3.9 2H-TaS_2 2D flakes transferred over FIB drilled holes (Scale bar is 10 μm) 45

3.10 High resolution SEM images of nanoindentation probes 46

3.11 Deflection versus piezo distance curve (for correction of virtual deflection) while AFM tip is in air 47

3.12 Deflection versus piezo distance curve while AFM tip is in hard contact with surface 48

3.13 Thermal spectrum showing vertical deflection of cantilever and simple harmonic oscillator (SHO) fitting to resonant frequency peak 49

3.14 AFM force distance curve regimes 51

3.15 Tip positioned in the center for Nanoindentation 51

3.16 Schematic illustration of Nanoindentation method, deflection of AFM probe when pushing down over suspended 2D material. Indentation δ is measured using equation mentioned below. 52

4.1 Optical microscope images (a) 3R-NbS_2 (b) 2H-TaS_2 (c) 1T-$NbTe_2$ (d) 1T-$TaTe_2$ crystals transferred over FIB drilled holes using viscoelastic stamp technique 55

4.2 Schematic illustration of (a) Rayleigh (b) Stokes (c) anti-Stokes Raman scattering 57

4.3 Raman profiles of metallic (a) 3R-NbS_2 (b) 2H-TaS_2 (c) 1T-$TaTe_2$ (d) 1T-$NbTe_2$ ultrathin flakes 58

4.4 Raman profiles of V_2O_3 phases 59

4.5 CPD maps [(a) and (c)] and CPD profile distribution measured from CPD maps of Au surface [(b) and (d)] 60

4.6 (a) Optical image of V_2O_3 flake with Au contact and silver epoxy connection (b) AFM topographical image (c) AFM height profiles from previous image 62

4.7 (a) CPD map of V_2O_3 flake (b) CPD profiles from previous different region in image 63

4.8 (a) AFM probe striking against SiO_2 64

4.9 (a) 2H-TaS_2 optical image with scale bar 10 μm (b) related topography (c) height profiles 65

4.10 (a) 2H-TaS_2 flake zoomed-in topographic image suspended over hole showing strong clamped behaviour (b) schematic before and (c) after indentation 66

4.11 (a) Force versus indentation of 2H-TaS_2 sheets with fitting (red crosses show breaking point of sheets that gives breaking stress) (b) log graph showing liner and cubic region at lower and higher loads respectively 67

4.12 (a) 2D pretension (b) prestress of $2H - TaS_2$ flakes 68

4.13 Elastic properties of 2H-TaS_2 flakes: (a) In-plane modulus (b) bulk Young's modulus against thickness 69

4.14 (a) AFM image of 2H-TaS_2 flake after fracture in center (b) F-D curve steps explanation 71

4.15 (a) Before indentation pristine tip radius 10 nm (b) after indentation image shows broadening in radius 72

4.16 (a) Before indentation pristine tip radius 10 nm (b) after indentation image shows broadening in radius 72

4.17 Optical microscope images of (a) 3R-NbS_2 (b) 1T-$NbTe_2$ (c) 1T-$TaTe_2$ ultrathin flakes (Scale bar is 10 μm) 73

4.18 Comparison of Young's modulus and breaking strength of metallic TMDCs's 74

4.19 Comparison of ultimate strain values and ratio of E^{3D} to breaking strength of metallic TMDCs's 75

List of Tables

4.1 Table 1 summarizes comparison of elastic properties of 2D materials 77

Chapter 1

Introduction

1.1 Brief Historical Introduction of Two Dimensional Materials

In 1959, during his visionary lecture entitled " There is plenty of room at the bottom," Professor R.P. Feynman explained feasibility of nanotechnology even that time word "nanotechnology" was not invented [1]. Although, nanotechnology department did not existed during that time, and Feynman was one of the few scientists to look and predict comprehensive potential of this field in his famous talk. Today, almost 60 year later we are all surrounded by nanotechnology.

With graphene exploration in 2004 [2] that gave Nobel price to K.Novoselov along with A.Geim, since then many researchers started focusing on 2D materials for example, graphene and TMDCs (transition metal dichalcogenides). Before this in 1980s some attempts were made using intercalation techniques [3] to isolate the layers which were stacked together by van der Waals forces. Later researchers from Columbia and Manchester university worked on thinning down the graphite layers. Columbian researchers used atomic force microscopy (AFM) based graphite tip (nanopencil) scribbing while Manchester researchers got successful exfoliation using simpler scotch tape cleavage technique.

Before 2004, isolated graphene was obtained from bulk graphite using mechanical cleavage technique and this method was used for many years. Mermin-Wagner studies [4] revealed, these 2D material's flakes are unstable due to fluctuation in long wavelengths and obtaining graphene was difficult task. After 2004, graphene showed new path to researchers with its unique electrical, chemical, physical, optical, thermal and mechanical features [5][6]. Graphene has astonishing electrical mobility (upto 250000 cm^2/Vs) [7], high Young's Modulus value (1 TPa) [8] and excellent thermal conductivity (5000W/mK) [9] as well as relativistic Dirac dispersion, universal and broad optical absorption [10]. Due to these excellent features graphene has many potential applications like gas detection, conducting electrodes or channels, energy storage gadgets, field effect transistors, photodetector, solar cells, nano composites, DNA sensors, liquid and gas separation [5][11].

Also, Samsung and IBM were taking enormous interest in graphene and mass production of it to use as a transistors with an idea to increase number of transistors in processors. But, limited mass production issue and with band gapless graphene based transistors yielded low ON/OFF ratio and perished hopes of replacing silicon (Si) with graphene in the processors. Despite of carrying excellent nanoscale features, this gapless character limits usage of graphene especially in logical electronic operation. Then there were two ways to sort out this problem, first was band gap opening using top-down technique by introducing defects whereas second option is to look for analogous materials [12].

In 2005 other 2D layered materials known as transition metal dichalcogenides (TMDCs) had been mechanochemically exfoliated. In 2011, first 2D n-type MoS_2 transistor was fabricated [13]. Although electron mobility of TMDCs was relatively low but ON/OFF ratio value was much larger because of significant band gap around 2 eV. TMDCs are combination of group-VI (transition metals with chalcogens) with formula MX_2 as M(Mo, W, Ta) is transition metal and X(S, Se, Te) and one transition atom is sandwiched by two chalcogenides. Different combinations among transition metals and chalcogenides are studied in literature, almost more than 40 types are existing [14]. These MX_2 combinations have covalent bonds in plane, whereas neighboring layers are stacked via weak van der Waals interactions same like bulk graphite. So, due to weak interlayer force, it

is easy to exfoliate them in mono, bi or even to few layer structure using scotch tape [15] .

Figure 1.1: Position of transition metals along with chalcogenides in periodic table

Copyright Permission Springer (2019) [16]

TMDCs are promising contestants for modern electronics and device fabrication because of significant band gap, atomic scale thickness and outstanding broad spectrum of electronic, optoelectronic mechanical [8] optical [17] and thermal [18] properties, especially 2D semiconductors play crucial role in scaling down dimensions of transistors and prove end of famous Moore's law [19]. Many potential experimental and theoretical studies had been carried out on the investigation of mechanical attributes of 2D materials especially semiconducting materials. Ultra-thin semiconducting TMDCs MoS_2 [20][12], $MoTe_2$ [21], WS_2 [22] and WSe_2 [23] has manifested exceptional mechanical features (Young's modulus, breaking strength and intrinsic strain) nominating them as a suitable contestants for mechanical devices, flexible electronic, transducers as well as nano-electromechanical systems. But future flexible electronics will demand not only thin flexible semiconductors but also metallic materials. This fact motivated us to map mechanical features of metallic TMDCs.

1.2 Thesis Goal

The aim of this thesis is to study atomically thin materials by atomic force microscopy(AFM). For this purpose, we chose multi functional Asylum force microscope and performed Kelvin probe force microscopy (KPFM) and Force distance spectroscopy (Force-indentation) on various atomically thin materials like, Vanadium Sesquioxide (V_2O_3) and ultrathin metallic TMDCs like, Tantalum disulfide (2H-TaS_2), Tantalum ditelluride (1T-$TaTe_2$), Niobium disulfide (3R-NbS_2) and Niobium ditelluride (1T-$NbTe_2$) respectively. KPFM studies explain work function measurement and force indentation studies revealed mechanical features like: Young's Modulus, pretension, stiffness and breaking or fracture strength of metallic TMDCs.

1.3 Atomic Force Microscope Details (AFM)

In 1980, scanning probe microscopy (SPM) was invented. In this SPM class, sharp probe is scanned over surface to sense nanoscale surface features. In 1981, one milestone was achieved with an advancement of Scanning tunneling microscopy (STM) [24] STM was first technique to provide 3D topographical images with atomic resolution, also continuously used for individual atoms manipulation to fabricate unique structures. But big limitation of STM is, it requires conductive sample for analysis. Afterwards, in 1986 AFM came into scientific field and revolutionized the scanning microscopy field [25]. AFM uses a sharp tip (radius less than 10 nm) for scanning therefore it is more advanced, developed and comprehensive version of STM that can image approximately many kind of surface at atomic scale resolution.

Since its invention, AFM has significantly evolved into a useful technique for wide spectrum of practical applications Like: direct analysis of micro-structural surfaces, study of nanoscale intermolecular forces with atomic scale resolution

[26], helpful in mechanical nanoindentation [8], electrical, piezoelectrical and electromechanical studies [27] as well as high resolution surface topography, roughness and thickness determination of CVD grown 2D materials and there are many others.

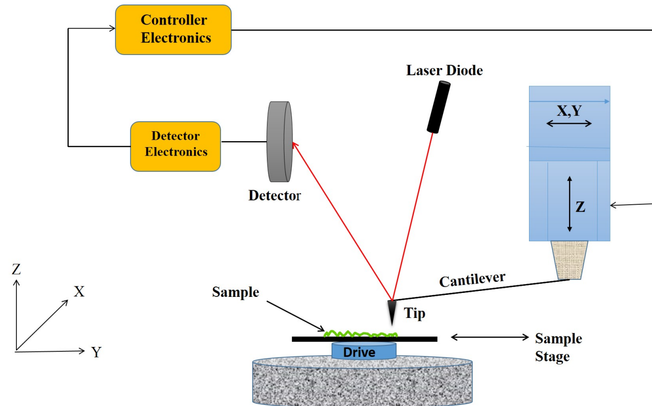

Figure 1.2: AFM schematic setup

Operation of AFM is based on detection of attractive/repulsive forces between AFM tip and sample surface. AFM tip is made of flexible cantilever which is responsible for signal transduction. Interaction of tip and surface makes cantilever bending or twisting in a way proportion to interaction force. Small laser diode spot focuses over cantilever, senses any twist or bending of attached cantilever. Any deflection of laser beam is read on segmented position-sensitive photodetector(PSD). During scanning deflection of cantilever because of surface features is monitored and then translated into a 3D image of surface [27][28].

1.3.1 AFM Operational Modes

AFM has multitude of various operating modes for different type of applications since its invention. Details of modes is given below.

1.3.1.1 Static Mode

Static mode also known as contact mode or constant force mode was first operational mode invented in 1986 [25]. Here, AFM tip is in continuous contact with sample. AFM cantilever tends to show deflection when tip comes in contact with the sample. And deflection of cantilever is measured with high precision via photodetector. Feedback loop makes cantilever's deflection constant through vertical piezo actuator adjustment [27].

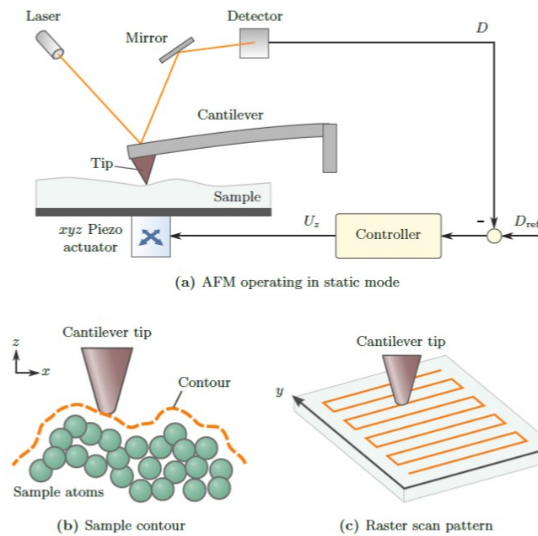

Figure 1.3: (a) AFM Static mode working principle (b) tip follows contour path (c) tip scans sample in raster pattern

Copy Right Permission from Author [29]

Then sample is scanned in lateral direction, usually in raster pattern. When deflection is constant, tip follows contour of surface of sample. Finally, by mapping lateral position against vertical piezo position, topographic view of sample is made. In static mode, deflection of cantilever is proportional to interaction force between tip and sample using Hooke's law [29].

Advantages to use this mode are, high scan speed, high atomic resolution is achievable. A challenge of using this mode comes because of high shear and lateral

forces (also frictional force) arising during scanning, and can damage both tip or sample (fragile like: biological) [27][30]. Also sharp tip may cause delamination, destruction and removal of material from surface. Also, soft cantilevers snaps with the surface of sample because of tip and sample attractive force, which makes feedback loop instable [31]. These challenges are major motivation to develop AFM dynamic mode [26].

1.3.2 Dynamic Mode

In 1990, dynamic mode also known as AC mode, tapping mode, intermittent contact mode (tip taps on sample surface) or non contact mode (tip never touch sample surface) invented to address demerits of static mode [27]. In this mode, cantilever oscillates at its mechanical resonance frequency using dither piezo spotted at base part of cantilever. Amplitude, frequency and phase of deflection automatically adjusted as cantilever comes closer to sample. So, deflection is demodulated, and kept constant in feedback loop, and constant tip-sample distance is kept at set point [32]. Then just like static mode, tip scans sample in raster pattern to show its topography.

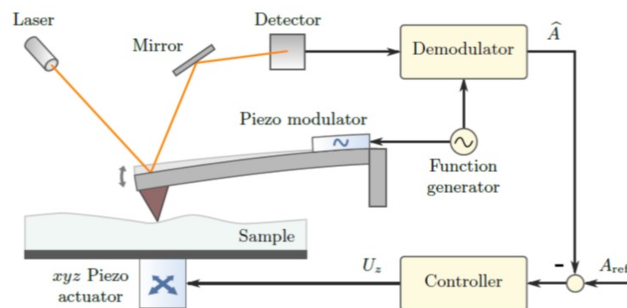

Figure 1.4: AFM Dynamic mode working principle
Copy Right Permission from Author [29]

During scanning, this mode minimizes friction and low force is applied to sample surface that results in no damage of tip and sample especially soft samples[30]

[33]. Relatively lower lateral resolution as compare to contact mode because of tip-sample distance.

1.4 Revealing Electrical and Nanomechanical Properties

Recent advancement in technology has transformed AFM into powerful nanoscale technique which is not limited to topographic analysis only but provides a plenty of information about low-dimensional materials, like: mechanical [8], chemical [34], electrical [35], optical and electrochemical properties [36].

1.4.1 Electrical Properties

For nanoscale devices, surface scanning properties like: current, surface potential variation, capacitance and conductance are crucial parameters imaged by AFM. For the measurement of these nanodevices' properties, multi-purpose AFM has programs named as Kelvin probe force microscopy (KPFM), conductive AFM (C-AFM), piezoelectric force microscopy (PFM) and electrostatic force microscopy (EFM). All these electrical measurement functions use specialized tips, normally conventional silicon cantilever with some kind of electrically conductive layer or uniform coating. AFM probes made from conducting diamond can be useful for some of these methods. These electrical functions take advantage form dual pass scanning method and interlaced, in which tip first measures topography and then during second pass it performs electrical measurements at defined lift height in order to avoid from cross talking or contact electrification phenomena especially for KPFM [35].

In this thesis we will use KPFM technique to map contact potential difference between AFM probe and sample to evaluate work function of the sample using capacitance circuit idea given by Lord Kelvin in 1898 (comprehensively explained

in second chapter) [37].

1.4.2 Nanomechanical Properties

Mechanical feature of two dimensional crystals play crucial role in many applications of flexible electronics. As electronics is heading towards miniaturization meanwhile flexible electronic gadgets have attained immense interest and two dimensional material are favorite candidates because of ultrathin nature and high flexibility [20]. Apart from mechanical properties measurement, applied strain along with external forces is capable of modifying crystalline structure of graphene and TMDCs while affecting their lifetime and performance of their devices in flexible electronics [38]. Also, mechanical stretching and releasing is used to change lattice structure of a material to regulate its electrical and optoelectronic features to get numerous piezo response.

AFM probe is capable for measurement of interaction forces present between probe and sample with high precision because of highly sensitive cantilever-laser geometry. AFM is not limited to map topographical features only but it has ability for analyzing high precision mechanical response that has made AFM an astonishing tool for determination of the nanomechanical characteristics of a material[39]. AFM uses nanoindentation mode for quantitative characterization of material's mechanical properties using well shaped, sharp tip as an indenter against sample's surface.

In this thesis, we investigated mechanical properties of ultrathin flakes of metallic TMDCs using nanoindentation technique which measures force versus distance curves to further explain mechanical features.

1.4.2.1 Force-Distance Curves (F-D)

AFM force distance (F-D) curve is a comprehensive plot of tip and sample interaction forces against tip and sample distance. To obtain such a F-D plot, the

sample surface (or tip) gets ramped along vertical axis and deflection of cantilever is acquired. Resulted interaction force is explained by Hook's law ($F = -k_c\delta_c$). Whereas, acquired distance is the vertical distance lies between surface of sample and cantilever's rest position [40].

Using same concept, this rule can be used for analyzing the mechanical properties of various samples, just by slowly indenting sample surface by AFM tip and measuring the deflection of cantilever and sample. Some elastic features like: adhesion, stiffness, fracture strength and Young's modulus of sample can be analyzed through yielded F-D curves [41][42]. Complete description of F-D curve is shown below,

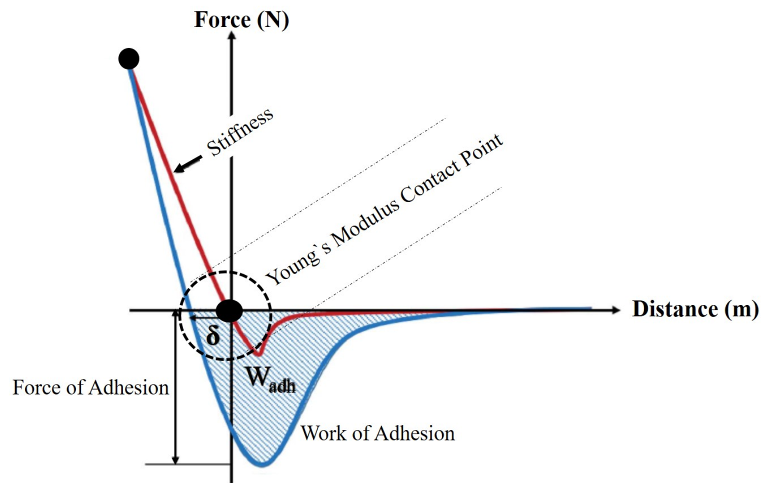

Figure 1.5: AFM Force-distance curve depicting various interaction regions Reproduced [43]-Published by The Royal Society of Chemistry

1.5 Outline

This thesis have five chapters and categorized in three parts. An overview of 2D materials is explained in this chapter along with comprehensive explanation of AFM. Following this first chapter, chapter 2 explains major background information from literature about extensive AFM applications which are performed

on atomically thin materials. Furthermore, chapter 3 is responsible to explain experimentation along with materials and methods. In closing, results and discussions for both Kelvin probe force microscopy (KPFM) and force-indentation will be explained in chapter 4. Whereas conclusion and remarks for future work are presented in chapter 5.

Chapter 2

Extensive literature survey of KPFM and Nano-Indentation

2.1 What is Work Function?

In solid state physics, work function is minimum energy or thermodynamic work needed for taking an electron out from crystal to vacuum level point is most fundamental feature of surface of a material [44]. In detail, work function is energy difference of two states of a crystal. During initial state, crystal having N electrons assumed in the ground state having energy E_N. During final state, one electron comes outside of crystal and supposed to be lying at rest having zero interaction with image.It has electrostatic potential energy explained by vacuum level (E_V).

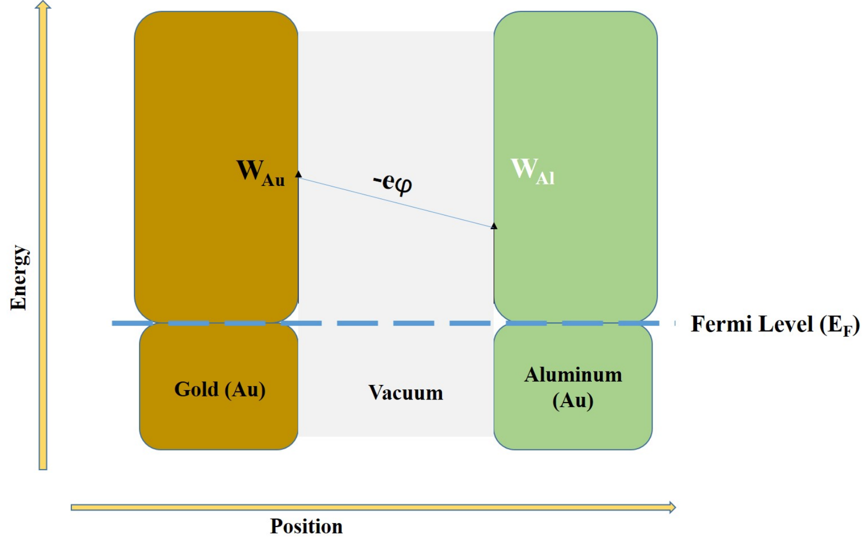

Figure 2.1: Band alignment comparison of two metals
Reproduced [44]

$$W = -e\phi - E_F \tag{2.1}$$

And crystal having N-1 electrons is still at ground state having energy E_{N-1}. This condition is valid for only zero temperature case as well as perfect vacuum because crystal remains at ground state after and before removal of electrons. The idea of work function first came in 1935 given by Bardeen.

$$\phi = (E_N - 1 + E_V) - E_N \tag{2.2}$$

E_V shows electrostatic potential energy related to removed electron which is at rest, lying near vacuum point with no interaction. If crystal is infinitely large homogeneous, its E_V will be at infinite distance to the crystal surface [45].

This is immensely sensitive to subtle variations in composition, structure and contamination /alteration of chemical and physical features of surface of crystal [44][46]. For example, nanoparticles of gold (Au) within size dimension 3-10 nm are metallic while their wave function also changes from bulk because of electrostatic effects [47][48].

2.2 Measurement of Work Function: Experimental Techniques

Work functions can be measured through various experimental methods and also using theoretical calculations. Following are few of techniques to calculate work function of materials.

2.2.1 Method of Diode

In 1935 this method was proposed by Anderson [49] . Here, a cathode source is heated and electron's beam targets anode on a sample, and this beam is electrically accelerated. This beam has atomically large size but compare to crystal surface it is small. Resulted current will be measured against difference of potential between electrodes. There will be horizontal shift in I-V, if sample's work function changes. Normally, feedback circuit fixes current, that allows variation of work function linked with applied potential. If beam generated through electron gun and bombarded to sample, one can scan it across substrate and map work function [50]. This method has been vastly used in gas adsorption over metallic surfaces in situ analysis [51].

2.2.2 Kelvin Probe Method: Contact Potential Difference (CPD)

Kelvin probe force microscopy (KPFM) is combination of non contact AFM and Electrostatic force microscopy (EFM) using Kelvin probe concept or technique. Lord Kelvin first gave this idea in 1898 for analyzing surface potentials: sample comprises of one plate attached with parallel plate capacitor having another plate with known metal that is vibrated on certain frequency [37]. Due to alternation of distance between attached plates, capacitance varies, yielding an ac current in circuit holding the plates. This current value is reduced upto zero through

applying dc-voltage value to one plate. This Voltage value corresponds to contact potential difference (CPD) between two materials, therefore this technique known as Kelvin probe (KP). KPFM employs same electrical technique applying dc voltages to adjust CPD value between sample and AFM probe [52]. However, electrostatic force is used as controlling parameter instead of current. AFM CPD method gives a way to calculate work function of sample, with reference of some metal. This method relies on existence of difference of potential between two metals which are connected electrically.

When electrically connected, there will be flow of electron from material having low work function towards higher one, this will continue unless both materials has same electrochemical potential. This will re-align Fermi levels making system thermodynamically in equilibrium. This flow will yield difference of potential between metals that is called as contact potential difference V_{CPD} or CPD. This CPD is equivalent to initial difference in work function existing before establishment of contact between sample and tip. Measurement of induced electric field between two electrodes gives CPD value. When measuring this CPD value, this electric field needs to be nullify by applying an external DC voltage V_{DC} among electrodes. Once electric field gets nullified, V_{DC}=V_{cpd}. Finally, work function can be measured like this:

$$\phi_2 = \phi_1 - eV_{DC} \tag{2.3}$$

Through this procedure, one should know the AFM probe work function calibrated earlier (Referenced work function) [37].

Majorly this technique focuses on measuring differences of work function, either between different kinds of materials, can work in air and vacuum both yields surface topography along with work function with respect to already defined standard material work function [53]. KPFM measures work function via calculating contact potential difference (CPD) among two materials (tip and sample). Fig 2(a) explains energy levels of both sample and AFM probe when there is no electrical path between them. There is an association of vacuum levels but vital mis-alignment found between Fermi levels. Equilibrium required alignment of Fermi levels, if AFM probe and sample are sufficiently close for electrical link.

Fermi levels tend to align through electronic current flow, therefore system attains equilibrium state depicted in Fig. 2(b). This alignment yields potential between them (Sample and probe). If applied voltages V_{DC} is same like V_{CPD} with opposite sign then electric force will be diminished by applied voltages giving CPD value as clear in 2(c) [54][55].

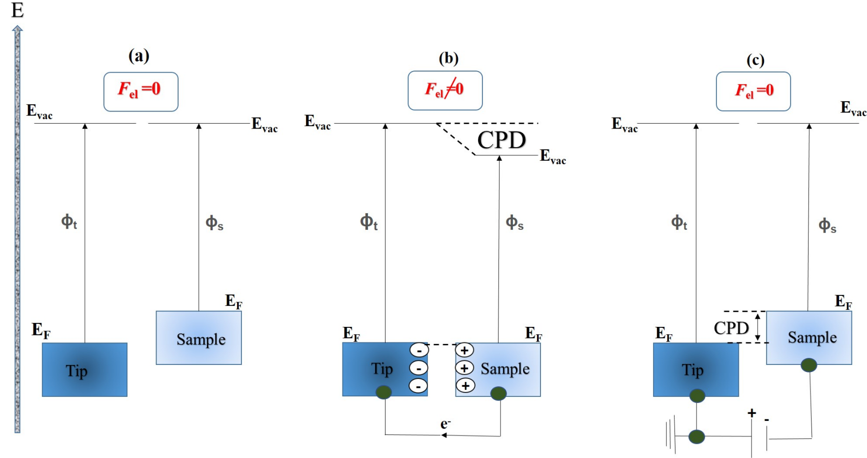

Figure 2.2: Mechanism of KPFM. (a) two metals having different values of work functions come into contact (b) Fermi level alignments (electron flow from less work function metal to higher untill CPD generates because of build in electric field) (c) external potential needed to nullify CPD (re-alignment of Fermi levels) Reproduced [56]

Ideally, KPFM probes electrochemical potential for sample lying under tip apex using this relation [57].

$$V_{cpd} = (\phi_{tip} - \phi_{sample})/e \tag{2.4}$$

where e stands for electron charge. For all this, one should know work function of tip before scanning targeted sample through calibration of tip method using any surface which has stable work function value as reference. Highly oriented pyrolytic graphite is best option for calibration of probes. It has work function value in air around 4.475 ± 0.005 eV [56], but one can use gold coated samples to calibrate the AFM tip as well [58].

AFM based microscopic technique named as Kelvin probe force microscopy (KPFM) is regard as powerful route to image the electrostatic forces, distribution of electrical potential at high nano metric resolution [59]. In 1991, Nonnenmacher invented KPFM [60]. This technique has various names, like as scanning Kelvin microscopy (SKM) [61], scanning Kelvin probe microscopy (SKPM) and scanning Kelvin force microscopy (SKFM) [62]. This technique works for analyzing material science aspects like: work function findings [60], charge transfer and finding surface potential of p-n junctions of silicon [63], potential measurement for the resistors along with $n - i - p - i$ hetrojunctions [64].

2.2.2.1 Dual-pass Operating Mechanism of KPFM

For better analysis and measurement of CPD and to avoid from contact electrification one should use KPFM in lift mode that comprises of two tracing steps that are interleaved. Interleave meaning, they are tracing one line at a time along with both pictures showed on screen together and cantilever goes twice over each line in image. During first step, AFM traces only topography whereas in second step CPD is measured but line by line [35].

- **First Trace for Topography**

  In this trace, AFM uses tapping mode to image surface topographical view of single line over surface. The cantilever oscillates mechanically close to resonance frequency via small piezoelectric unit with no additional voltages to AFM tip. Therefore, short range van der Waals interactions dominates the long range electrostatic interactions.

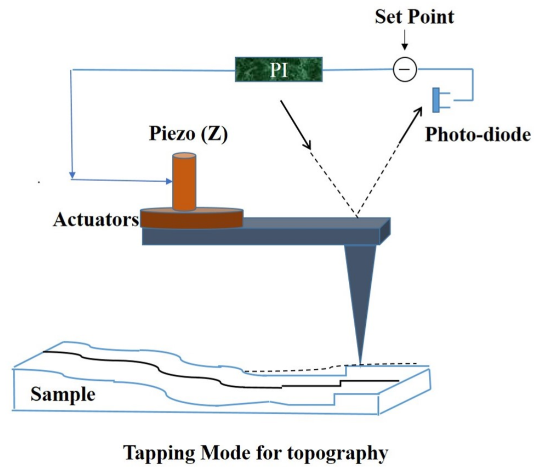

Figure 2.3: First trace for topography
Reproduced [65]

- **Second Trace for CPD Measurement**

  During this step, AFM tip is set at some height or lift height distance approximately between 10-50 nm over same line on sample surface following contact electrification mechanism [35].

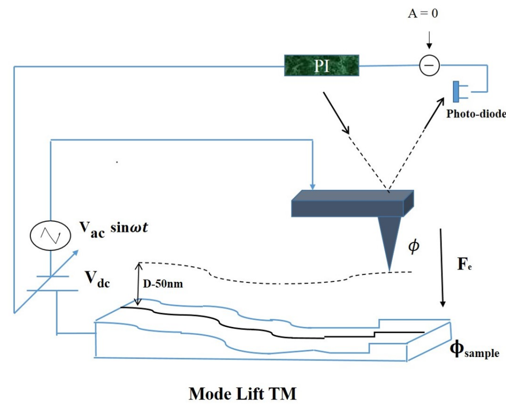

Figure 2.4: Second trace lifting of tip to detect electrostatic forces at surface
Reproduced [65]

For this lift up mode, mechanical excitation for cantilever becomes off and now an ac voltage around 2-3 V will be applied to tip at resonance frequency

of cantilever.

$$V_{bias} = V_{dc} + V_{ac}Sin(w_e t) \tag{2.5}$$

where V_{ac} known as sinusoidal voltage amplitude and V_{dc} is direct voltages (feedback loop will use these voltages for tip to nullify the value of electrostatic interactions) also, ω_e called as electric driving frequency.

CPD presence yields an additional value of potential drop means V_{cpd} present between AFM probe and sample having different work functions. Then total difference of potential lying between sample and AFM tip is as:

$$V_{ts} = (V_{cpd} + V_{dc} + V_{ac}Sin(w_e t) \tag{2.6}$$

2.2.2.2 Electrical Force

This potential difference V_{ts} yields electrical force between AFM probe and sample which causes tip oscillations. The expression for electrical force is obtained by derivative of electrostatic energy for capacitor system that is formed through AFM probe and sample: here, C_{ts} is capacitance, Z is distance between probe and sample and this derivative was obtained during constant voltages. The expansion for this equation gives three different components:

$$F_{dc} = \frac{1}{2}\frac{\partial C_{ts}}{\partial z}[(V_{cpd} + V_{dc})^2 + \frac{1}{2}V_{ac}^2] \tag{2.7}$$

$$F_{we} = \frac{\partial C_{ts}}{\partial z}(V_{cpd} + V_{dc})V_{ac}sin(w_e t) \tag{2.8}$$

$$F_{2we} = \frac{-1}{4}\frac{\partial C_{ts}}{\partial z}(V_{ac}^2 cos(2w_e t)) \tag{2.9}$$

As F_{dc} does not depends upon time and it makes static bending for cantilever and relies on two factors: first, applied voltage values and secondly gradient value of capacitance C_{ts}. While other two components (F_{we} and F_{2we}) are time modulated and induce cantilever vibrations or oscillations at same frequency value just as driving signal also second harmonic.

These force components, second harmonic value F_{2we} is present whenever V_{ac} is non zero while first component F_{we} is present when V_{cpd}=V_{dc}.

2.2.2.3 Feedback measuring CPD

In order to evaluate and conclude CPD value during lift mode, the oscillations of AFM cantilever are noticed by locking signal at this frequency w_e. Afterwards, feedback loop tries to adjust direct voltages V_{dc} for canceling oscillations of cantilever and therefore F_{we} is nullified and V_{dc} voltages becomes equal to V_{cpd}.

$$V_{dc} = V_{cpd} \tag{2.10}$$

Therefore, during second trace V_{dc} voltage is continuously observed. Finally, CPD values between AFM probe and sample can be analyzed continuously [57][65][66]. Then simply after this complex process one can use the below equation for calculation of work function of material.

$$V_{cpd} = (\phi_{tip} - \phi_{sample})/e \tag{2.11}$$

2.2.3 Work Function of Vanadium Sesquioxide (V_2O_3)

For future electronics and device fabrications ultrathin graphene and TMDCs attracted immense attention of scientists around the globe but there are other atomically thin material which are capable of performing at nanoscale electronics. Recently in our group at SCM Lab UNAM we published a study based on synthesis of Vanadium Sesquioxide (V_2O_3), this material is of great concern about half century because of having pressure-temperature phase diagram. V_2O_3 has three phases, paramagnetic metal (PM), anti ferromagnetic metal (AFI) and thirdly paramagnetic insulator (PI) [67]. V_2O_3 undergoes phase transition (MIT) from paramagnetic metal form to the anti ferromagnetic insulator when temperature decreases upto 155 K leading to great physics features variation.

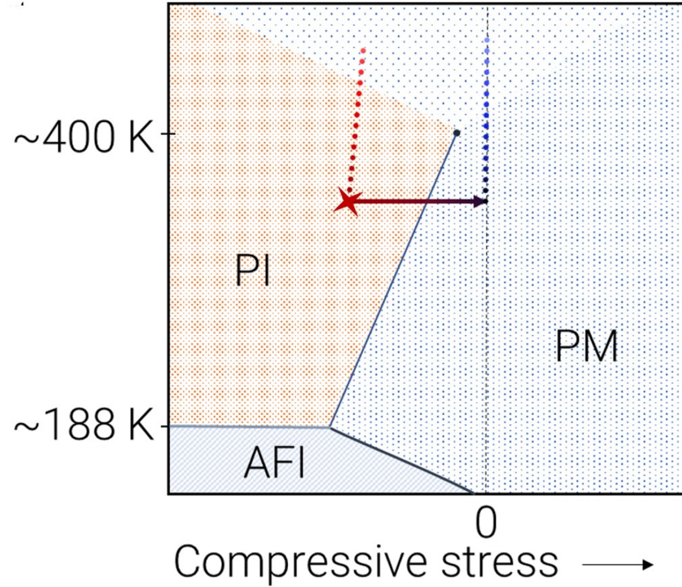

Figure 2.5: V_2O_3 Pressure-temperature picture
Copyright Phys. Rev. B (2019) [68]

Below 188K, AFI having monoclinic structure of crystal is stable [69]. Like VO_2, MIT temperature for V_2O_3 is important in presence of few dopants along with implementation of pressure. Indeed, increment in pressure, doping of titanium, presence of extra oxygen all contributed to decrease temperature for MIT [70]. Moreover, MIT can occur without the relevant changes present in phase while when dopants of chromium are present, makes insulating phase stable [71].

This phase diagram has been extensively studied. For electrical device performances, nature of contacts between metal and V_2O_3 is crucial issue to understand for fabrication of future devices based on V_2O_3. In nanoscale experiments and device performance, larger difference in work function value between analyzed material and metal contact yields reasonable Schottky barrier height (SBH) present at interface and lead to high contact resistance that will affect electrical performance of nanoscale devices [72]. As V_2O_3 is atomically thin like TMDCs, therefore knowing and calculating its work function is crucial because one can

choose appropriate metal electrode contact with work function values closer to work function of V_2O_3 to reduce SBH.

2.3 Determination of Mechanical Properties of TMDCs

Using an AFM nanoindentation technique, some of mechanical features (Young's modulus and pre-tension) of suspended metallic TMDCs with wide thicknesses range were measured.

2.3.1 Young's Modulus

Modulus is numeric value which represents physical feature of material and reaction of any material to applied external forces. Young's modulus (E) value is mechanical characteristic of material that depicts stiffness and strength of material and explained as ratio between stress σ and strain ϵ [73].

$$E = \frac{\sigma}{\epsilon} \tag{2.12}$$

Stress (σ) is explained by force (F) applied at unit area (A),

$$\sigma = \frac{F}{A} \tag{2.13}$$

While, strain (ϵ) is ratio between elongation $\varDelta$L in material versus original length (L),

$$\epsilon = \frac{\varDelta L}{L} \tag{2.14}$$

Relationship between stress and strain is explained through the figure mentioned down, two regions are depicted in the picture, one is linear and other one is non linear, these two regions contribute towards calculation of elasticity modulus [74].

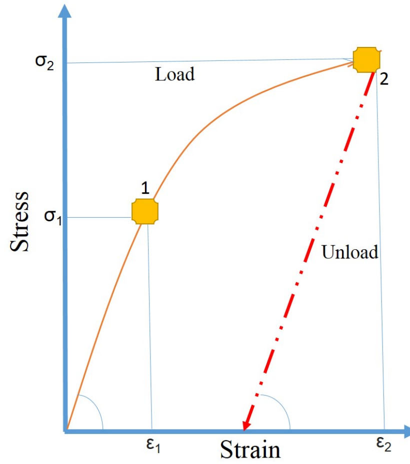

Figure 2.6: Stress-strain relationship diagram consisting of two regions Reproduced [74].

Elastic characteristics are crucial determinants for TMDCs strain engineering and play haughty role in designing flexible 2D nanodevices [22]. There are literature reports revealing excellent mechanical features of 2D materials like: ultrahigh in-plane value of elastic modulus as well as extra-ordinary breaking strength unlike their conventional three dimensional counterparts. For example, monolayer of graphene is stiffest material which possess an ultrahigh value of Young's modulus around 1 TPa and have ability to carry stress upto 25 percent limit without breaking. This much stiffness is because of in-plane covalent bonds between carbon atoms [8].

Having high Young's modulus, strain value, excellent breaking strength atomically thin materials can withstand against large strains untill inelastic relaxation, fatigue or rupture occurs [75][76]. As elastic modulus gets numerous attention and key factor for determination of mechanical characteristics of 2D materials and played pivotal part recently in optoelectronic, stretching and flexible electronics applications [77]. Their excellent stiffness and good flexibility have played vital role in flexible resonators, transistors and oscillators [78].

Elasticity is basic mechanical feature of 2D materials, it plays significant role

in device application as well as in strain engineering. Ability to tune material's features is most unique characteristics of 2D crystals. This is because of atomic thickness, an electronic and optical characteristics of such materials highly sensitive for external perturbations [79]. Modifying electronic characteristics of material using mechanical strain has become a powerful technique to improve efficiency of many electronic devices. This methodology has been implemented with high ratio to atomically 2D thin materials having great technological potential [80].

Investigation of mechanical properties of semiconductor TMDCs like: MoS_2 [75], $MoTe_2$ [21], WS_2 [22] and WSe_2 [23] is done already. So, we decided to chose metallic TMDCs those which are not explored mechanically, will be analyzed through AFM to reveal their mechanical properties experimentally.

2.3.2 Metallic TMDCs ($\mathbf{MX_2 : M = Ta, Nb - X = S, Te}$)

For the investigation of mechanical properties of metallic TMDCs we chose Tantalum and Niobium based four compounds as: Tantalum disulfide (2H-TaS_2), Tantalum ditelluride (1T-$TaTe_2$), Niobium disulfide (3R-NbS_2) and Niobium ditelluride (1T-$NbTe_2$). 2H-TaS_2 in bulk form, is composed of covalently bonded sulfur and tantalum planes stacked over each other. Below we depicted crystallographic structure of 2H-TaS_2 one of four metallic TMDCs.

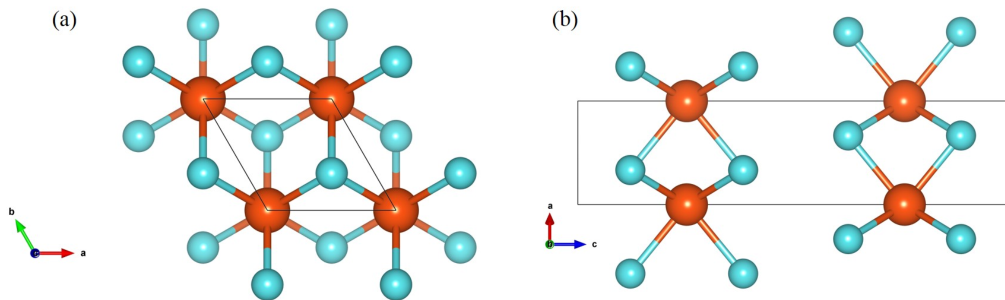

Figure 2.7: 2H-TaS_2 Crystal structure (a) top (b) side view

2.3.3 Metallic TMDCs Mechanical Properties Measurement Method

There are various techniques to measure mechanical properties in the literature, but we used AFM based nanoindentation technique as this method is robust to measure elastic properties for graphene and other TMDCs. Comprehensive details of the method are as,

2.3.3.1 Nanoindentation

Besides imaging, AFM has key feature to map surface mechanical characteristics like stiffness, fracture and adhesion through force distance (F-D) curves. Using an AFM in force-indentation mode an AFM probe act like an indenter, and depends upon spring constant "K" also depending upon strength of tip vertical forces ranging between micro newton (μN) to pico newton (pN) can be analyze. With this force sensitivity of picoNewton and spatial nanometric resolution AFM provides a powerful platform for observation of intermolecular forces at level of single molecule and imaging topographical view [81]. Nanoindentation is best method for testing mechanical characteristics of materials that has been used for both graphene and TMDCs.

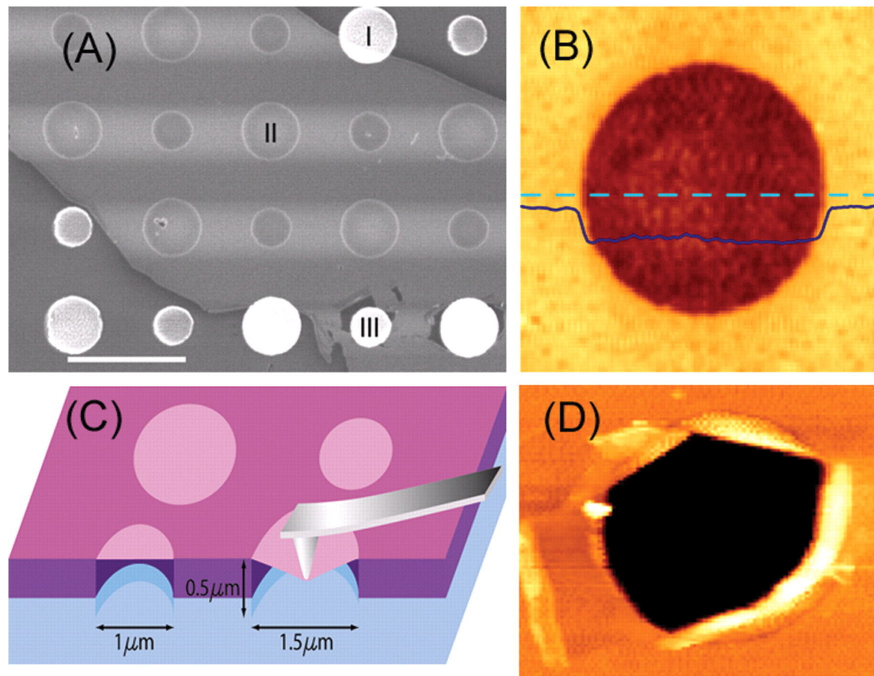

Figure 2.8: (A) SEM image of suspended graphene over holes (B) Non-contact mode topographical image of graphene flake over hole (C) Schematic setup for nanoindentation (D) Fractured topographical image after maximum indentation Copyright (2008) Science [8]

This route for indenting suspended 2D materials using AFM tip as nano-indenter for measurement of mechanical properties was first introduced by Lee *et al*, they suspended monolayer graphene for this study as shown above [8].

AFM is not limited to image topography with high resolution for solid surfaces, it has ability to measure the F-D curves as illustrated below. These curves provide useful information about mechanical features of material like: elasticity, Young's modulus, hardness, adhesion and breaking strength [8][75]. And use of these force curves has extended in numerous application of science in the area of material engineering, biology and surface science [39].

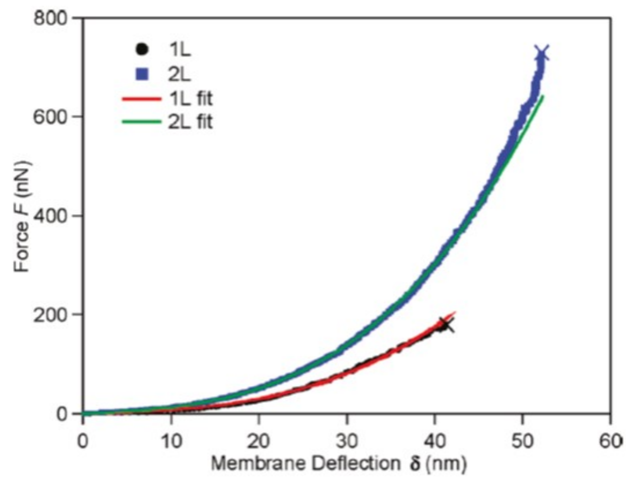

Figure 2.9: Force-deflection curves for monolayer and bilayer MoS_2
Copyright (2011) ACS [75]

In this thesis, F-D curves measurement for 2D materials will be done by suspending them over holy substrate (SiO_2) and AFM probe will apply force at the center of suspending region as shown below.

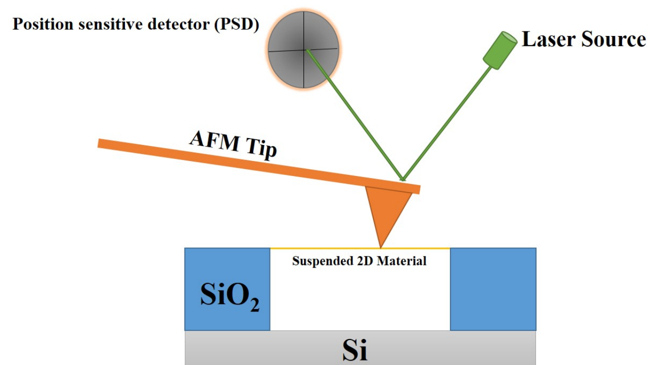

Figure 2.10: AFM based nanoindentation schematic

2.3.4 Analysis of F-D curves using Continuum Mechanics Model

Continuum mechanics model for suspended TMDCs sheets or flakes over circular holes is comprised of relationship between the force which is being applied at center of suspended crystal and corresponding deformation in flake. Therefore, suspending flake over circular hole considered as isotropic elastic flake and is tightly attached to substrate along with its perimeter and will be treated as clamped flake having some pretension values because of Van der Waals interaction between flake and substrate. Force versus deflection relationship considering suspended circular flake or nanosheet facing point force load exactly at center can be explained as Model 1: [12][21][82][83].

$$F = \frac{4\pi E^{2D} t^3}{3(1-v^2)R^2}\delta + (\sigma_0^{2D}\pi)\delta + [E^{2D}\frac{q^3}{R^2}]\delta^3 \tag{2.15}$$

Here, F is applied load or point force acting at center, δ is subsequent indentation depth or deflection from center of suspended flake against applied force, E^{2D} is in-plane modulus, thickness of flake is t, radius of underlying hole is R, σ_0^{2D} is already present tension in membrane, q known as dimensionless constant [22] evaluated by using defined Poisson's ration ν of crystal following this formula;

$$q = \frac{1}{1.05 - 0.15\nu - 0.16\nu^2} \tag{2.16}$$

In continuum mechanics formula, first term is linked with bending behavior of thick suspended flakes with specific bending rigidity (F$\sim\delta$) and mostly valid when thicker flakes need to be indent (thickness should be $>$ 15 nm) [21] [84]. For thicker flakes, bending rigidity dominates (because of having its cubic dependence on thickness t^3) on other two terms that are going to be linear under high deformations even [12][20][85][86][87].

Second term is linear (F$\sim\delta$) part that illustrates the contribution coming from stretching of 2D flakes associated with pretensioning response (σ_0^{2D}) and valid under small applied loads (proportional to thickness) [8]. It is crucial to note the existence of σ_0^{2D} in TMDCs suspended flakes that arises due to interaction

between underlying substrate and transferred flake.

$$F = (\sigma_0^{2D}\pi)\delta \tag{2.17}$$

And finally the third term is associated with nonlinear stiffening (F$\sim\delta^3$) of suspended flakes because of tension that is induced by deflection.

$$F = [E^{2D}\frac{q^3}{R^2}]\delta^3 \tag{2.18}$$

This term dominates under high applied force and large deflection of suspending flakes and relies only on Young's modulus as well as geometrical factors. So, summing up all the contribution we have model which governs mostly mechanical behavior of plate instead of membrane or nanosheet can be used to characterize elastic response and provides comprehensive estimation of σ_0^{2D}.

$$F = k_{bending}\delta + K_{pretension}\delta + K_{stretching}\delta^3 \tag{2.19}$$

If thickness of suspending crystal or nanosheet is less than 15 nm [84] and very low as compare to radius of underlying hole, there comes transition from plate to membrane regime. Because thin flakes show forces versus indentation traces highly nonlinear in the beginning ignoring thick plate behaviour. Therefore, first term in main equation that corresponds to bending rigidity behaviour of plates becomes invalid [8][88][89][90].

Thus, summing the total contribution of mechanical pre-tension in flake (linear behavior for small loads) and large-displacement expression (non linear under high loads) for thin TMDCs flakes can be written as Model 2:

$$F = (\sigma_0^{2D}\pi)\delta + [E^{2D}\frac{q^3}{R^2}]\delta^3 \tag{2.20}$$

Applied load gets balanced by pretension in suspended flake and varies linearly with the vertical deflection [22]. Under small loads they are characterized via liner relationship of force and indentation and that force changes linearly against displacement. And when load is increased and increment in indentation depth δ it is ruled by stiffness of crystal with cubic relationship and in-plane value of elastic deformation dominates. This happens when applied load is heavy enough and stress becomes significantly greater against pretension of flake, the F-D relation

tends to follow cubic relationship. This part will be taken into analysis of layers stiffness during applied force cycle that makes force deflection F(δ) nonlinear [12][75] as shown in figure above illustrating two distinct parts.

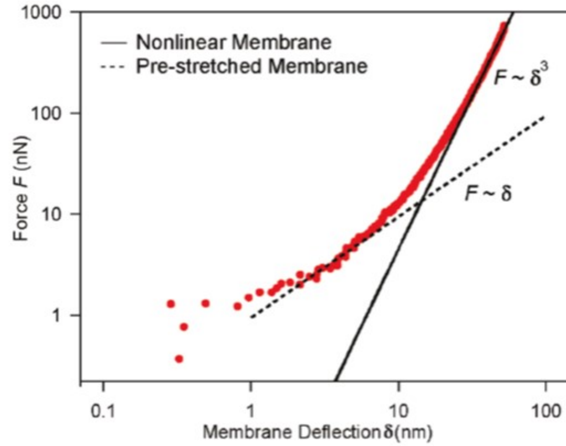

Figure 2.11: Loading curve showing linear and cubic regimes under different forces Copyright ACS (2011) [75]

Obtained F-D curves data will be fitted by using above continuum formula comprises of linear and cubic terms utilizing least square tool for fitting of curve considering E^{2D} and σ_0^{2D} like free parameters. And in order to compare 2D elastic features against bulk counterparts, in-plane modulus E^{2D}, pretension σ_0^{2D} will be divided against thickness of suspended TMDCs flakes to have normal or volumetric Young's modulus (E^{3D}) and prestress respectively [8][82][91] .

So keeping in view both above expressions for thick and thin suspended flakes, one can conclude there will be transition form linear to non-linear regime for force curve traces when thickness of flakes gets decreased. There is vital difference between these two models, so thin flakes act as suspending membranes (here one neglects bending rigidity and tension dominates) while on other hand thick flakes consider as plate like behaviour (dominated factor is bending rigidity and tension gets negligible) and this transition is perfectly visible in the F-D curve traces for mica in the figure below [20].

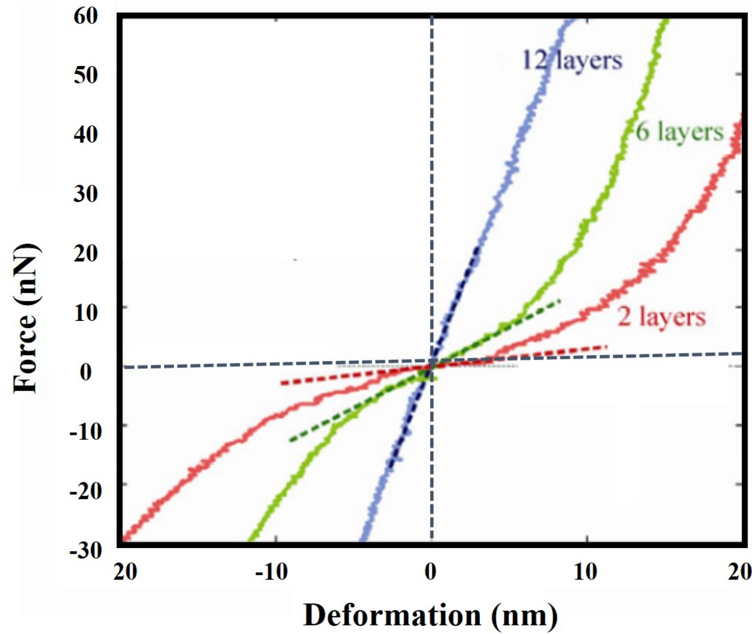

Figure 2.12: FD Curves for mica showing non-linear behave for 2-6 layer while 12 layers showing linear trend under applied load

Reproduced with Copyright Nano Research (2012) [20]

Here, thin flakes (2-6 layers) depict non-linear traces under applied force and can be explained by model 2 while 12 layers can not be explained using same model as bending rigidity value is so high therefore shows linear trace in response to applied load. To explain this, one should take bending rigidity into consideration for calculation of Young's modulus and pretension.

2.3.4.1 Measurement of Breaking Stress and Strength of Suspended Flakes

As point load theory produces stress singularity at center of suspended 2D flake, it is pivotal to consider indenter geometry to quantify maximum stress coming from indenter tip. Maximum value of tensile stress that corresponds with fracture

strength of each flake suspending over circular hole and indented through spherical shape indenter can be analyzed through linear elastic response of suspended flake. And one can know and measure fracture or breaking strength (σ_m^{2D}) of 2D suspended flakes. As force reaches to breaking point, then suspended crystal collapses. Therefore during nanoindentation testing with spherical shape indenter maximum stress value for circular and linearly elastic sheet as a function of maximum point force can be illustrate as: [23][82][92][93].

$$\sigma_m^{2D} = \sqrt{\frac{F_{max} E^{2D}}{4\pi R_{tip}}} \tag{2.21}$$

Here, σ_m^{2D} and F_{max} are maximum stress on central part of flake (right under AFM tip) and fracture or breaking force respectively, R is AFM probe's radius and is known quantity from sellers and even one can measure it through SEM images of AFM probes and E^{2D} is 2D elastic modulus. Thus, breaking stress for suspended flake can be figured out by acquiring maximum force which can break 2D flake during indentation. Considering maximum stress value for 2D materials, this has linear relationship with maximum strain value. That breaking or maximum strain formula is,

$$\epsilon_m = \frac{\sigma_m^{2D}}{E^{2D}} \tag{2.22}$$

Finally, same like Young's modulus and prestress one can have 3D breaking strength by dividing maximum breaking strength against the thickness of corresponding flake.

In general, 2D flakes will be suspend over holes and through sharp AFM probe load will be exerted in the center of suspending region resulting in subsequent deflection of flake. Segmented Position sensitive photodetector (PSD) is responsible for collecting laser light deflected from cantilever after indentation.

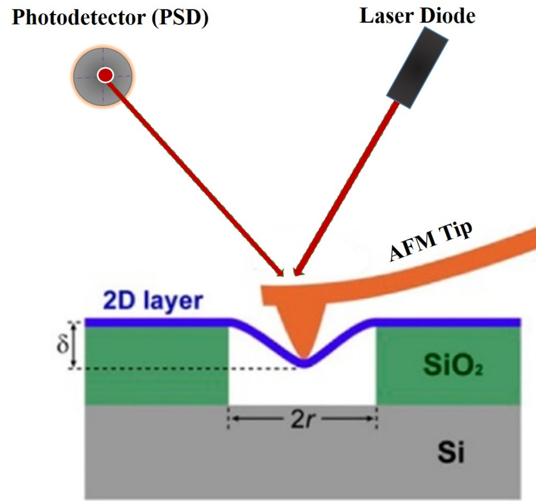

Figure 2.13: AFM nanoindentation block diagram
Reproduced and Copyright ACS (2014) [75]

As a result of controlled indentation AFM software gives raw data that can be process further in MATLAB and origin to calculate in plane 2D elastic modulus E^{2D} and pretension σ_m^{2D} values. We will use above mentioned least square fitting model to fit our F-D curves for the calculation of Young's Modulus, pretension values of suspended flakes further in this thesis in next chapters.

Chapter 3

Experimental Protocols

This chapter mainly focuses on experimental parameters and techniques that were used to carried out the research as well as comprises of comprehensive explanation of synthesis of materials, routes to prepare samples and methodology for performing experiments.

3.1 Instrumental description

AFM equipment that we used for testing both electrical and nanomechanical features of atomically thin materials is commercially available. All of experimentation in this thesis performed in UNAM Microscopy Lab, Bilkent University Ankara Turkey. Commercially available Asylum atomic force microscope (AFM model MFP-3D Asylum research equipped with vibration controller and isolation system) have various functions to work on. We used KPFM and Nanoindentation modes of AFM for our atomically thin material's characterization. Variety of other supporting equipments are also used available at Strongly Correlated Materials Lab UNAM and AFM setup is shown in the figure below.

Figure 3.1: Asylum AFM setup at UNAM

3.2 Experimentation for KPFM

KPFM, a nanoscale characterization technique which has ability to image the material surface contact potentials at nanoscale by high sensitivity along with lateral resolution. This technique has lengthy range of applications for characterizing electric/electronic features of metals, semiconductors as well as insulating materials [35]. However, this requires deep attention for measuring process and preparation of good sample with pure contacts. So sample preparation for KPFM comprises of below written steps along with other experimental tools introduction.

3.2.1 AFM Probes for KPFM

For KPFM measurement, conductive tips has to be used. The AFM probes for our studies were Arrow FMR-10 AFM probes (spring constant 2.8 N/m and resonance frequency 75 kHz from Nano world), these were coated with aluminum

but detector side only. So to make them conductive, we coated them using precision etching coating system (PECS) present in UNAM with Gold (20 nm) and Chromium (5nm) at slow deposition rate to make these probes conductive.

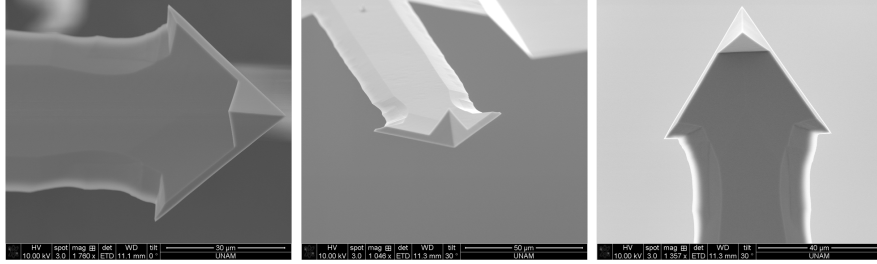

Figure 3.2: SEM images of KPFM probes

- **Calibration of AFM Probes** For KPFM, one need to calibrate the tip before using it and should know its work function value regardless if it is new or old as it can have some contamination, some residues or hydrocarbons some adsorbed molecules which may alter the work function of tip. Usually, AFM tip is calibrated against a surface having known value of work function.

  As gold (Au) work function is 5.1 eV defined in literature, so we took SiO_2 substrate coated with 200 nm Au through thermal evaporation and measured its contact potential difference (CPD) map against AFM tip using KPFM. Through CPD, we calibrated our work function of tips as M.Baghdad *et al.*, used gold as a reference material in his work [58].

  After evaluating CPD between two surfaces, we used following formula to define the work function value of our AFM probe.

$$V_{cpd} = (\phi_{tip} - \phi_{sample})/e \tag{3.1}$$

3.2.2 Sample Preparation for KPFM Measurements

For electrical contact potential measurement using KPFM needs grounding connection and good sample preparation as follows. First of all we selected chemical

vapor deposition (CVD) grown V_2O_3 flake using optical microscope at SCM lab UNAM. Then we took indium and melted it upto melting point (157 ^{o}C) and after that using micro manipulator with sharp needle setup we placed indium contact on V_2O_3. After placing indium connection to V_2O_3 flake we used silver epoxy for attaching an external electrical wire and placed it in ambient to get dry. Then we placed our sample on AFM stage and grounded it with another electrical wire coming out of AFM holder together with wire attached to V_2O_3 flake. After establishing pure connections, we performed KPFM measurements over it using Asylum MFP-3D AFM microscope scanning kelvin probe microscopy (SKPM) mode to map CPD profile (schematic shown below).

3.3 Mapping of Surface Contact Potential Difference (CPD) using KPFM

Below figure explains the schematic of the KPFM mechanism. Electrical wire is bonded with conductive silver epoxy and have direct connection with crystal through indium contact, while KPFM probe is suspended exactly on top at the device to interact with surface for inquiring both topography and contact potential difference (CPD).

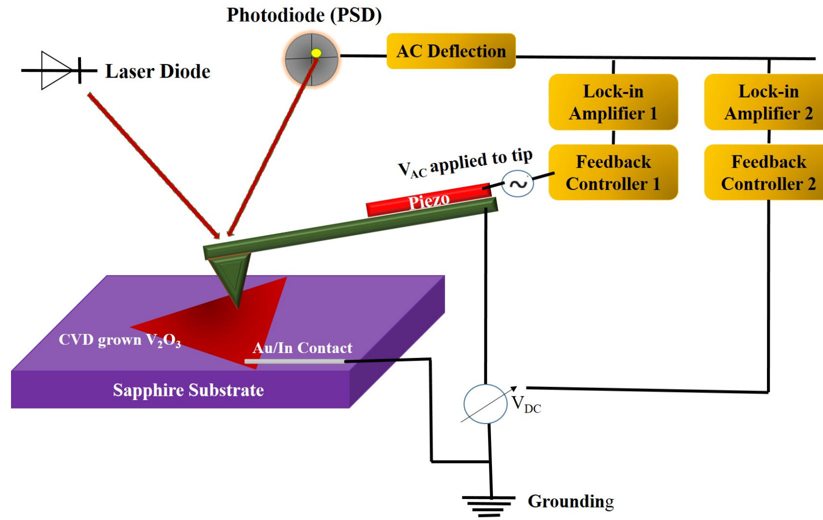

Figure 3.3: Schematic of Asylum KPFM setup

After preparing sample and calibration of AFM tip we imaged our prepared sample using dual pass amplitude modulation(AM) technique in KPFM. In the first mode, AFM probe worked to yield topographic features using tapping mode. Here during this mode, cantilever of probe gets excited near the value of resonance frequency along free amplitude right before tip gets closer to sample surface and feedback parameter is adjusted by set point amplitude for topography of a crystal. Then in second mode AFM probe lifts upto pre-defined certain height (ΔH=10-50 nm) in spectroscopic way for surface potential measurements. We changed this height difference from sample to sample. During this, potential feedback setup is responsible for surface potential scans.

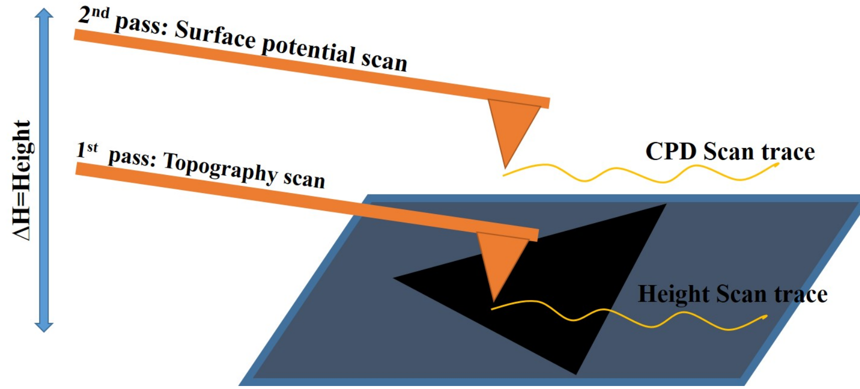

Figure 3.4: Sketch map for KPFM scanning process
Reproduced with Copyright (2016) ACS [35]

We provided an AC voltage of 3V to AFM probe and we did all our measurements in ambient environment. For these measurements, tip-sample electrostatic talk is minimized at every point on surface using bias voltages, this voltage later produces difference in work function between metallic probe and scanned sample [94].

In simple sense and wording usually in KPFM, AFM probe and surface of sample has different value of work function and upon electrical connection there occurs charge flow between them as Fermi levels tends to equalize, this is known as contact potential difference (also called CPD) as briefly explained in chapter 2.

AFM probe is biased through ac/dc voltages values (as schematic shows above). One lock-in amplifier attached with setup measures force component (detail in 2nd chapter) value with frequency (ω) of provided ac bias. Meanwhile on same moment, a feedback loop alters dc voltages values untill measured value of force becomes zero. Then, direct bias applied value becomes equal to measured surface potential (CPD) and we calculated work function of sample using this expression.

$$V_{cpd} = (\phi_{tip} - \phi_{sample})/e \tag{3.2}$$

3.4 Sample Preparation for Nanoindentation

To measure mechanical properties of TMDCs experimentally, one should fabricate suspended structure. These suspended structures could be of various shapes like, trenches, holes and some bridge type fabrication [78][95][96]. Our fabrication process comprises of several steps as mentioned below. We used holes on SiO_2 surface while following some experimental protocols to suspend our ultrathin flakes for nanoindentation.

3.4.1 Cleaned Holey Substrate Preparation via Focused Ion Beam (FIB)

To suspend our 2D ultrathin flakes over holes we tried several experiments to fabricate array of holes on SiO_2 wafer using FIB. FIB is extremely valuable gadget in nanopatterning, nanoscale welding and nanoscale fabrication of devices by creating various patterns. We used FIB technique present in UNAM for the purpose of drilling nanometric scale diameter holes. This FIB uses Gallium ion source for bombardment of ions. We used SiO_2 wafer as our target substrate, as this substrate is insulator so before exposing it to FIB we coated it with conductive polymer PEDOT:PSS using spin coater (rate: 2000 rpm) in order to avoid from charging in FIB.

Without coating with conductive polymer, we observed some shift in beam and it deformed the shape of our holes as well. We draw a pattern of holes with exact diameter 1 μm and depth more than 500 nm. The current value we used was 48-93 pA as using higher current will take less time for drilling but deforms the shape of holes from circular to ellipse or deformed holes. Below we have showed SEM pictures of our FIB drilled holes using serial milling technique.

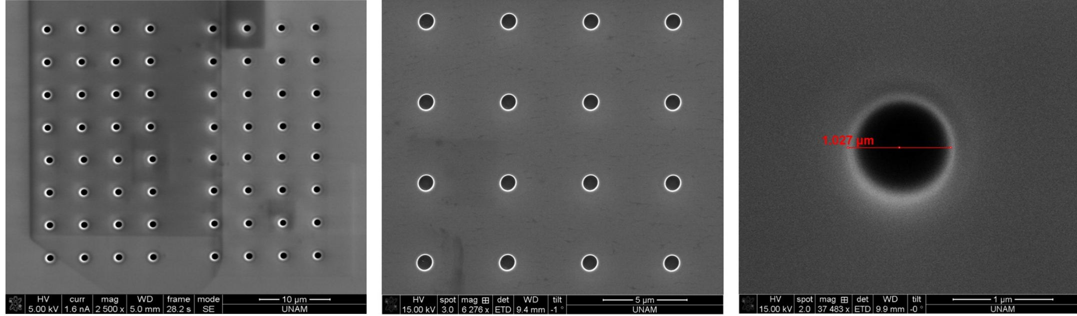

Figure 3.5: FIB drilled holes SEM images

3.4.2 Isolation or Fabrication of Ultrathin TMDCs

In the past, different fabrication techniques are used to isolate TMDCs thin flakes. Selection of suitable isolation method heavily relies on application area of related flake. As these fabrication techniques are different in yielding size, quality, thickness and texture of flakes. So we used following routes to get ultrathin flakes for mechanical nanoindentation according to feasibility.

3.4.2.1 Chemical Vapor Deposition (CVD) Synthesis of Niobium Disulfide (NbS_2)

CVD is promising and time-honored route to grow large area ultrathin TMDCs flakes that are hard to exfoliate. This is bottom up strategy where 2D TMDCs flakes are synthesized using their constituent precursors by thermal process. During CVD solid material gets deposit from the vapor via chemical reaction that occurs in vicinity of heated substrate.

NbS_2 flakes were grown using ambient chemical vapor deposition route on a c-cut sapphire substrate. Before growth, we washed sapphire substrates using acetone, isopropanol, water and dried them using N_2 gas. Niobium pentoxide (Nb_2O_5) powder, crushed salt (NaCl) and Sulfur (S) were used as a growth precursors and mixed them (Nb_2O_5 and NaCl) together using mortar. We used NaCl

to reduce the melting point of (Nb_2O_5) and aid the growth process. After we put this crushed mixture in an alumina boat and placed sapphire substrate facing down inside the boat (at very close distance to precursor) we also put Sulfur in another alumina boat. We placed Nb_2O_5 and NaCl mixture boat in central heating zone downstream from sulfur boat (sulfur melts around 115 ^oC so it was placed upstream from center at low temperature region inside the tube) in inner glass tube (as shown in figure).

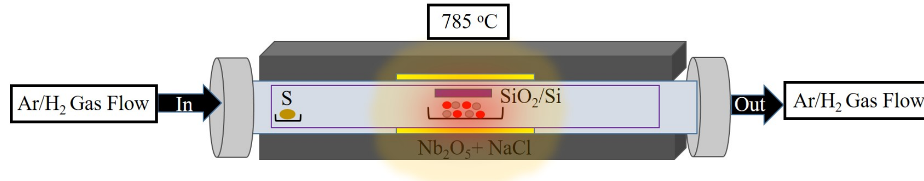

Figure 3.6: NbS_2 CVD growth setup

After sealing chamber, argon gas (flow rate of 499 sccm) was purged for 6 minutes to remove air inside the tube. After 6 minutes, we turned on the heater and set argon flow rate around 20 sccm and waited for temperature to reach at 785 ^oC. After achieving desired temperature, we set Ar/H_2 flow rate 100/12 sccm and then held there for 10-15 minutes (growth time). After that, H_2 was stopped and set argon flow at 20 sccm and opened the chamber to cool it upto room temperature.

- **Wet Transfer Method**

  We spin coated C-cut sapphire substrate having NbS_2 flakes with Poly(methyl methacrylate) PMMA 495 (A4) using 1300 rpm. Then we heated the substrate at 180 ^oC for 180 seconds. Afterwards, for 20 minutes we dipped the substrate in buffered oxide etch (BOE) to release PMMA film having CVD grown flakes from sapphire substrate. Then PMMA film was released in water through wedge transfer technique and picked up using PDMS stamp. Then we dissolved this film in acetone for 15-20 minutes to transfer NbS_2 flakes successfully. Finally, desired flake was transferred on FIB drilled holes using PDMS dry transfer technique as discussed below.

3.4.2.2 Exfoliation

For obtaining 2D flakes, previously discussed route was bottom-up approach, i.e., flakes were synthesized using related precursors and close chamber. This route is known as top-down approach or mechanical exfoliation to isolate 2D flakes form parent bulk layered source. TMDCs depict powerful intra-layer bonding of metal and chalcogenide atoms but feeble inter-layer connection bonding among neighboring chalcogenide atoms planes [97]. TMDCs use wan der Waals stacking to compile MX_2 material's mono layer that consist of transition metal atom (M) which is sandwiched by two other chalcogen atoms (X). Flakes of TMDCs are easy to cleave along layer plane because of weak forces called van der Waals existing between adjacent layers same like graphite. Individual mono layer or few layers are able to be isolated from bulk through micromechanical cleavage method or scotch tape which is used for obtaining graphene flakes from graphite [98].

We obtained bulk crystals from HQ Graphene (the Netherlands) except NbS_2 (as we did CVD growth mentioned above) and exfoliated using Nitto blue tape over Polydimethylsiloxane (PDMS) stamps for the transfer. Nitto adhesive tape is much convenient and reliable for exfoliation of 2D materials. The selection of tape is crucial as some tapes can contaminate 2D flakes or sometimes can break it into very small parts. Some of the 2D flakes images on PDMS are below and resulted images after dry transfer are shown in next section.

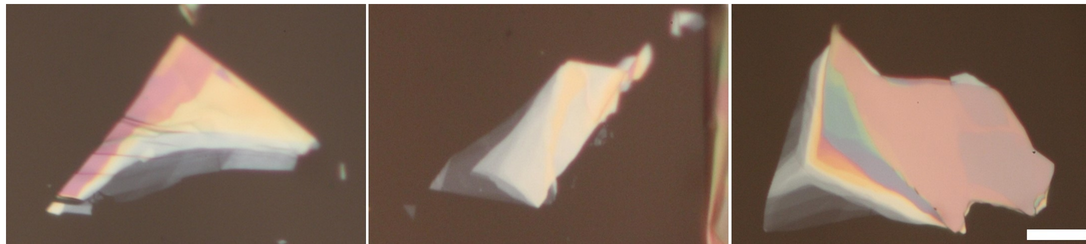

Figure 3.7: Optical images of 2H-TaS_2 exfoliated flakes on PDMS stamp (Scale bar is 10 μm)

- **Dry Transfer Method** Although direct exfoliation on prepatterend microwells is usable to place 2D crystal over holes randomly, but finding good

and suitable crystal is rare as well as adhesion traces will contaminate the sample and may contaminate AFM probe used in measurement. Therefore, one should use all-dry transfer route using polymer named Polydimethylsiloxane (PDMS) rather to use adhesive tape. For dry transfer technique, we did direct exfoliation of TaS_2 and other 2D flakes over PDMS stamp and peeled off PDMS stamp rapidly and checked exfoliation yield under optical microscope. Optical inspection shows direct exfoliation over PDMS yielded many crystals, as an interesting thin isolated crystal is found we transferred it over FIB drilled holes using homemade transfer setup in SCM Lab UNAM. The flake is transferred to holy SiO_2wafer having various patches of circular holes with 1 μm diameter and 500 nm depth just by pressing PDMS stamp against SiO_2 substrate and slowly peeling that stamp off. It will favor transfer of crystals from PDMS to holes over SiO_2 wafer surface as adhesion of wafer to flake is larger than to PDMS and that facilitates easy transfer.

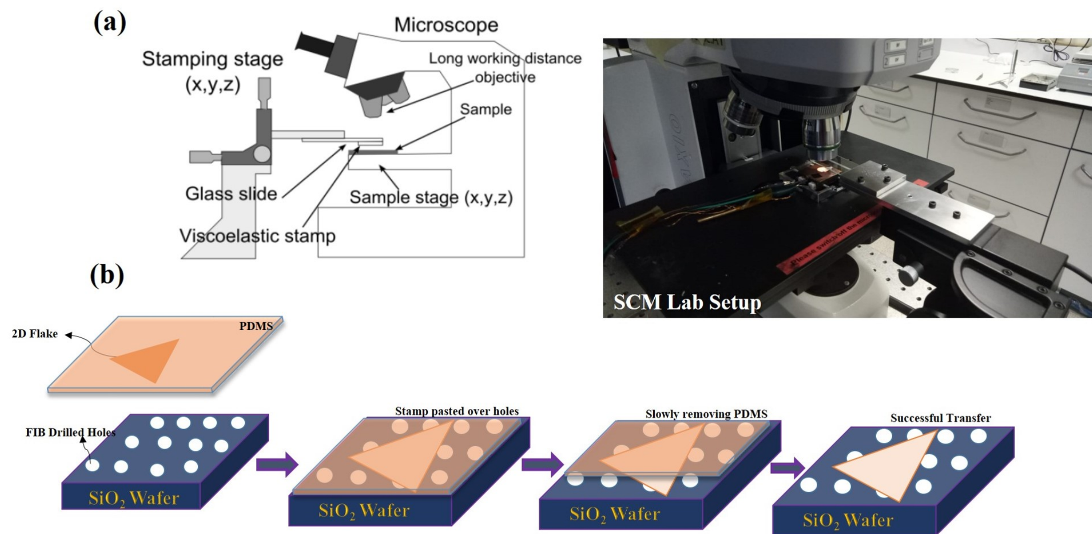

Figure 3.8: (a) Deterministic dry transfer method setup (b) procedure using PDMS viscoelastic stamp, inset shows SCM Lab dry transfer setup

Some of the 2D flakes transferred over holes using dry transfer technique are shown below.

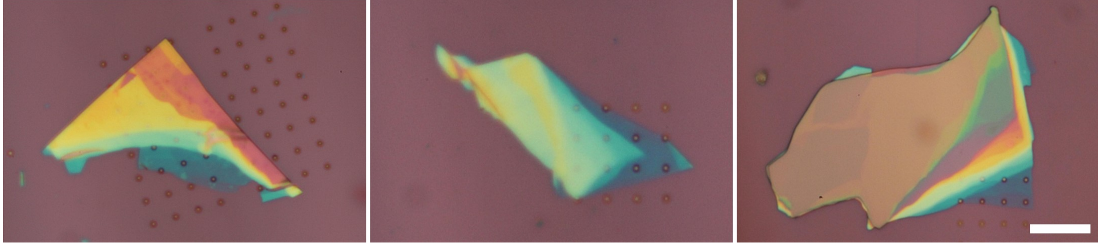

Figure 3.9: 2H-TaS_2 2D flakes transferred over FIB drilled holes (Scale bar is 10 μm)

3.5 Calibration of AFM Probes and Deflection Sensitivity

3.5.1 AFM Probes

It is crucial that suspended flakes spring constant should be closer to spring constant of AFM Probes. If tip used is too much stiff versus sample measured, then tip will not deflect at appropriate detectable amount. If AFM probe is too soft, then flakes will appear to be hard and rigid giving no meaningful information from measurement. As 2H-TaS_2 is hard material and other materials we analyzed they were thick so we used Tap300Al-G AFM probes bought from Budget Sensors with resonance frequency value 300 kHz and nominal force constant of 40 N/m . Tap300Al-G probes, has sufficient value of force sensitivity for nano-indentation as well as stiff enough for indenting and breaking of suspended flakes. This probe with radius less than 10 nm and 125 μm long cantilever was designed for force modulation experiments. It has 30 nm aluminum reflex coating towards detector side to enhance reflectivity of laser light.

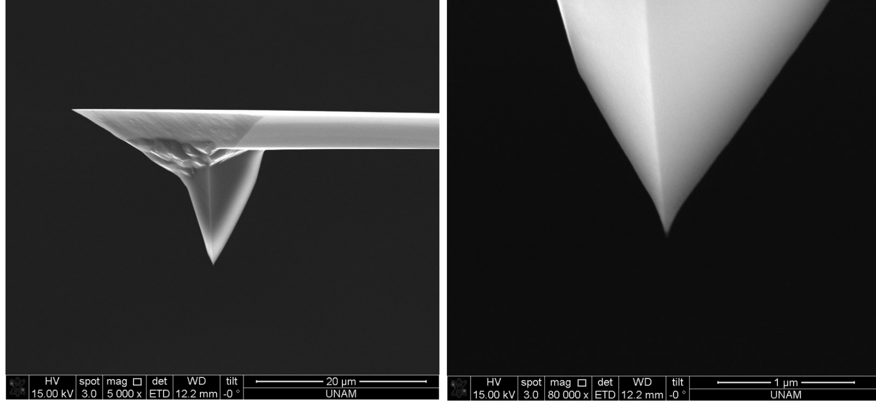

Figure 3.10: High resolution SEM images of nanoindentation probes

As spring constant of our probes is 40 N/m and this was calibrated also prior to indentation testing.

3.5.2 Calibration of AFM Probe's Spring Constant

Before calculation of F-D curves on need to calibrate spring constant for AFM cantilever and deflection or lever sensitivity or position sensitive detector calibration in order to acquire quantitative force measurements, true deflection and actual units. For spring constant calibration of AFM probes, we used built-in thermal method in Asylum AFM.

3.5.2.1 Deflection Sensitivity or PSD Calibration [Inverse Optical Lever Sensitivity (InvOLS)]

Deflection of AFM cantilever is detected through segmented position sensitive photodetector (PSD), this value is calculated in volts (δ_{volts}). To have deflection of AFM cantilever in nm, PSD should be calibrated and this calibration is done through cantilever deformation against hard surface so that lever deform as compare to surface, for this purpose we deformed our cantilever on clean SiO_2 surface. Then we noted direct correspondence between PSD measured voltages

and deflection of AFM cantilever. This is called as inverse optical lever sensitivity (InvOLS) [99] explained as:

$$InvOLS = \frac{dZ_{piezo}}{d\delta_{volts}} = \frac{nm}{V} \tag{3.3}$$

where, (δ_{volts}) is change in voltage values over PSD because of cantilever deflection.

3.5.2.2 Thermal Tunning Method for Calibration of Spring Constant

Determining spring constant using thermal method is three steps operation:

- **Correction of virtual deflection** that outcomes in AFM hardware system. This is mechanical coupling between cantilever deflection with upward movement of AFM piezo along Z-axis. This coupling comes from a concept how light aligned over cantilever when it travels via z-piezo range. This incorrect value yields minute slope in force curve as mechanical path may not be fully perfect. It should be corrected for accurate measurement and precise estimation for spring constant.

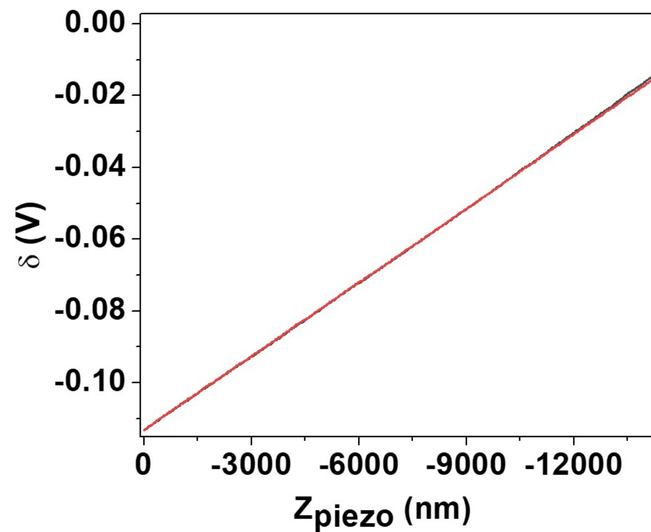

Figure 3.11: Deflection versus piezo distance curve (for correction of virtual deflection) while AFM tip is in air

- **Calibration of deflection sensitivity** by considering relationship between volts value analyzed when laser moves over detector (volts) and true deflection of cantilever (nm). Inverse of this sensitivity value will be taken for proper unit calculation and known as InvOLS. Also, in AFM we use optical lever comprises of laser, a cantilever and photodiode and one should convert photodetector voltages to real units. After correcting virtual deflection for force distance curves we brought AFM cantilever close to hard SiO_2 surface and deformed there.

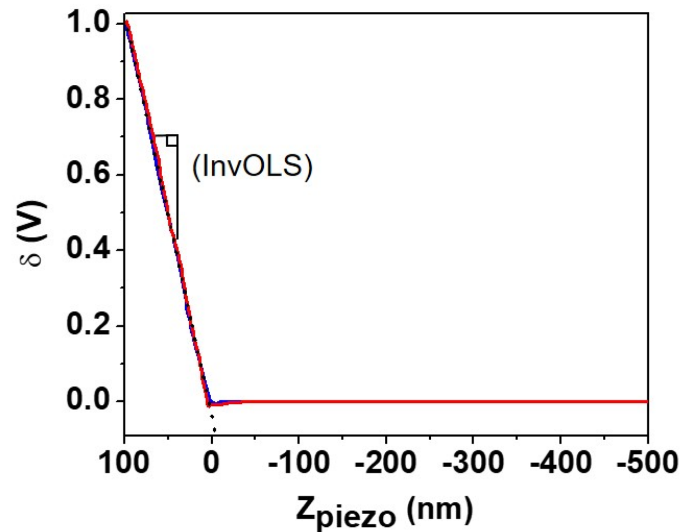

Figure 3.12: Deflection versus piezo distance curve while AFM tip is in hard contact with surface

InvOLS value is extracted from inverse value of slope of sample surface and AFM tip contact part. InvOLS basically describe an amount of PSD response (Volts) per cantilever deflection (nm)

- **Collection of thermal spectrum** by withdrawing of AFM probe and finding its resonant frequency and then afterwards through thermal fit one can have spring constant calibration. After having InvOLS, we withdraw AFM tip from surface and collected thermal spectrum of cantilever. This method records thermal fluctuations of AFM cantilever using diode laser

and tries to find frequency for main resonance of cantilever. During this process, thermal vibrations related to cantilever beam were recoded and AFM software plotted data by analyzing power spectrum of these thermal fluctuations. Then acquired spectrum (particularly resonant frequency peak) was fitted by simple harmonic oscillator fitting to evaluate spring constant. We found perfect analogy with reported resonant frequency as well as spring constant (mostly between 37-44 N/m) by AFM probes manufacturers.

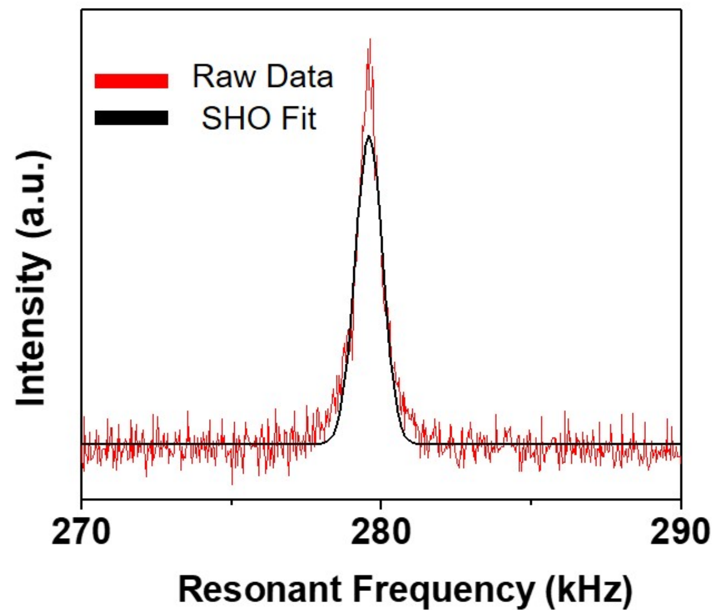

Figure 3.13: Thermal spectrum showing vertical deflection of cantilever and simple harmonic oscillator (SHO) fitting to resonant frequency peak

3.6 AFM Imaging and Nanoindentation

After locating our target flakes lying over circular hole, Asylum AFM operated in ambient at room temperature/pressure will act as nanoindentor. First, we obtained topographical features of our samples at nanometer resolution using AC air mode of Asylum AFM. We used AFM tapping mode to image topography

and surface morphologies as scanning through contact mode may damage the samples, for instance, suspended parts and tip degradation too. Also, scanning via tapping mode helps in finding indentation spot accurately [8]. The other advantage of using tapping mode for topography was to preserve and save tip radius from more degradation as radius is supreme contributor in the estimation of breaking strength of flakes.

During scanning, we observed thermal drift and we continued scanning the images for more than 1 hour until we get stable image. To avoid thermal drift we scanned a dummy sample under AFM for more than one hour before actual sample and that proved useful for us. After getting topographic scan we waited for few minutes in order to belittle thermal drift of AFM piezo actuators [8]. As thermal drift causes unwanted motion of AFM probe because of thermal contraction and expansion of piezo actuators in AFM. After this, we stopped scanning and changed AC mode to contact mode. Then, with help of this topographical image we chose suitable and good looking region (defects/wrinkle free, tears and contamination) containing our crystal for indentation purpose.

Also, we confirmed through topographical information that our suspended flake adhere with walls of holes upto several nanometers because of van der Waals interactions. After locating our hole

3.6.1 AFM Tip-Sample Interaction Steps

The process of indenting the our crystal comprises of distinct steps and AFM tip followed these strictly for accurate measurement. Firstly, at position 1 AFM tip is away from surface (means no interaction between them: constant deflection). Position 2 shows critical distance and AFM probe experiences the attractive force which snaps it to surface and deflection drops suddenly to negative value making (Z_{piezo}=0). At position 3, by further piezo scanner's extension, tip will deform the crystal surface while bending itself because of reaction force. This extension cycle lasts untill deflection attained predefined setpoint (point that defines maximum deformation in material). After this setpoint, retraction cycle will start, here

scanner start moving back by releasing strain in crystal. There comes a kink in curve during retraction, it appears because of adhesion between crystal and AFM tip while detaching and tip will leave surface hardly as one can observe attraction to surface at 5 number position [100].

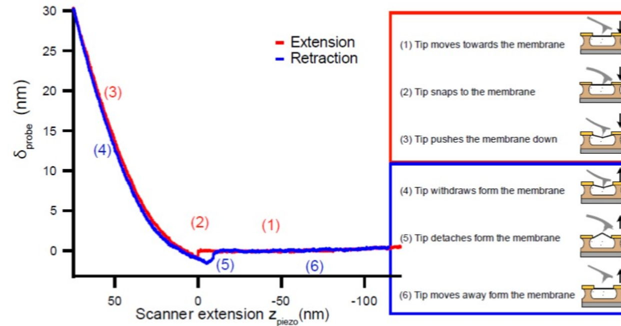

Figure 3.14: AFM force distance curve regimes
Copyright ACS (2015)

3.6.2 Nanoindentation

Next, after the scanning finished in tapping mode, we changed the mode to contact and AFM probe positioned at center of suspended flake over hole and gradually moved downward, getting controlled stretching for flake. And indented there to check subsequent deformation.

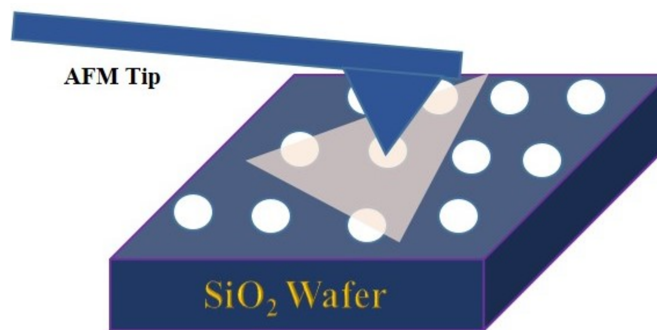

Figure 3.15: Tip positioned in the center for Nanoindentation

This subsequent deflection means suspended flake's deflection right from center where load is acting. During indentation, piezo scanner push stage towards cantilever with controlled speed and that Z_{piezo} displacement speed was controlled at 100 nm/s to get hysteresis free loading and unloading curves as well as to avoid possible damage of tip or suspended flakes. We repeated the loading cycles at one hole with increasing force upto rupture of suspending flake, then we reversed the load.

We indented our suspended flakes with force ranges (minimum 300nN-mechanical failure of flake occurs) and measured their elastic features. Mechanism of indenting is shown below in figures;

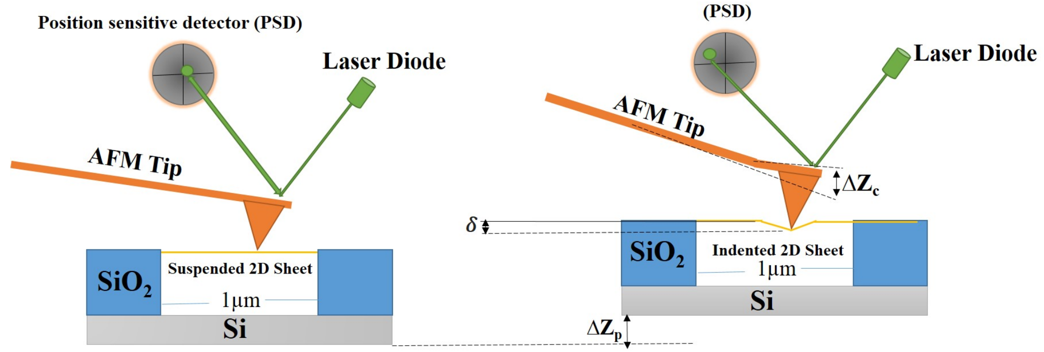

Figure 3.16: Schematic illustration of Nanoindentation method, deflection of AFM probe when pushing down over suspended 2D material. Indentation δ is measured using equation mentioned below.

When tip is in physical contact with crystal then elastic deformation δ, deflection in cantilever (ΔZ_c) and scanning piezotube displacement (ΔZ_p) are explained below through equation that shows relationship between applied load and related deformation or deflection of suspended 2D material [85][101].

$$\delta = \Delta Z_p - \Delta Z_c \tag{3.4}$$

Applied force on suspended flakes is directly related with cantilever deflection by Hook's Law.

$$F = K_c . \Delta Z_c \tag{3.5}$$

Here, K_c is spring constant (40 N/m) for cantilever being used in experiment. The nanoindentation of crystals lying over circular holes using AFM probe is convenient way to analyze elastic features and fracture nature of these ultrathin materials as nanoindentation avoids non-uniformity in strain as well as breaking near edges which is caused because of uniaxial stretch. Therefore, this technique of indenting ultrathin materials such as graphene and TMDCs has been used much [102].

After mechanical fracture and extracting our data sets, we scanned fracture area again to observe shape or fracture of flake.

Chapter 4

Results and Discussion

Nanoelectrically we performed KPFM to evaluate work function using surface potential variation on indium contacted CVD grown V_2O_3 ultrathin flakes. In nanomechanical context, we calculated elastic features of metallic TMDCs Like: 2H-TaS_2, 3R-NbS_2, 1T-$TaTe_2$ and 1T-$NbTe_2$ flakes having different thickness freely suspended over holes with 1 μm diameter using nanoindentation bending tests. During mechanical bending tests we performed experiment with AFM probe, and our measurements simultaneously allowed us to note in plane elastic modulus (E^{2D}), pretension (σ_o^{2D}), prestress, 3D Young's modulus (E^{3D}) and maximum value of breaking strength ($\sigma_m^{2D/3D}$) for metallic TMDCs. Prior to measurements and systematic analysis of both KPFM and nano-indentation, we performed several characterizations to know about scientific features of materials used. Detailed explanation is as mentioned below.

4.1 Identification/Characterization of ultrathin flakes

4.1.1 Optical Microscopy

As easiest technique for imaging sample is use of optical microscopy before further processing. Vanadium Sesquioxide V_2O_3 and metallic TMDCs flakes are able to be identified using simple optical/light microscope in our SCM lab. We used optical microscope company name Carl Zeiss present in SCM Lab having digital camera mounted on top of microscope to locate transferred samples over holes. Below are some optical images of metallic TMDCs and V_2O_3 images are shown under section 4.2.1.

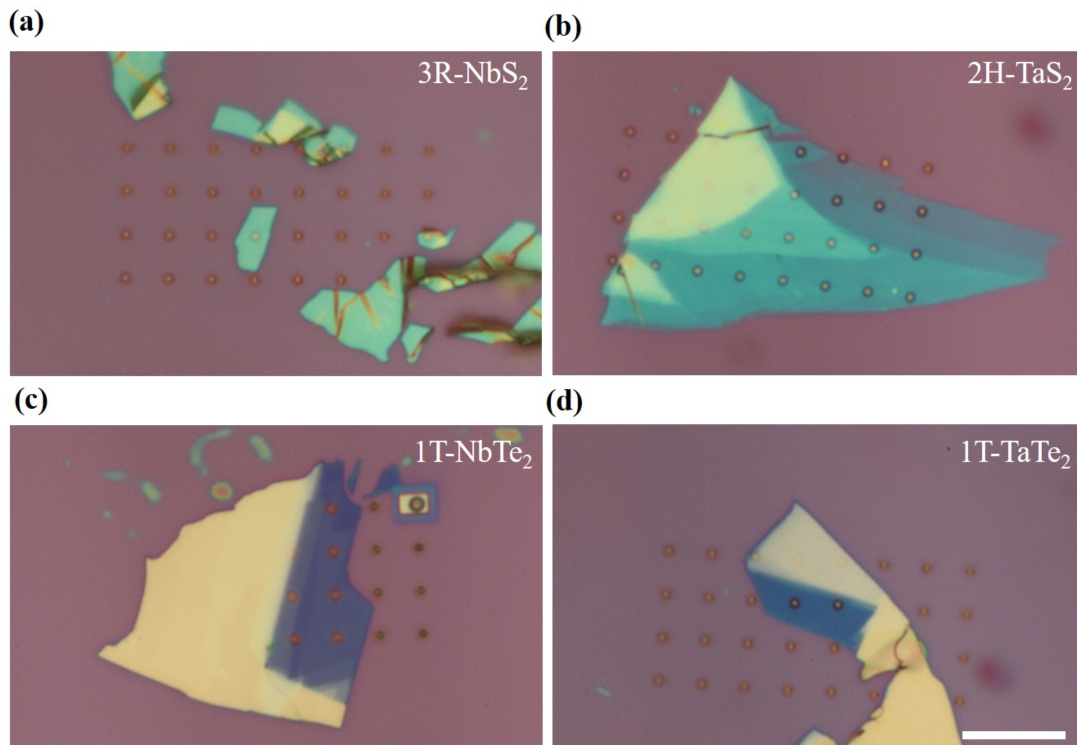

Figure 4.1: Optical microscope images (a) 3R-NbS_2 (b) 2H-TaS_2 (c) 1T-$NbTe_2$ (d) 1T-$TaTe_2$ crystals transferred over FIB drilled holes using viscoelastic stamp technique

4.1.2 Raman Spectroscopy

in 1928, C.V. Raman discovered Raman effect and got Nobel prize in 1930. Nowadays, Raman scattering effect is crucial characterization technique. We characterized 2D metallic ultrathin flakes using Raman spectroscopic setup to know about their chemical identification. Raman spectroscopy is used to observe vibrational, rotational, and other low-frequency modes in a system using monochromatic light source such as laser (visible or near-infrared). Raman uses laser because it is very intense beam of nearly monochromatic light that can interact with sample molecules. Usually the frequency of the emitted light is same as compare to frequency of incident light.

A laser beam is used to irradiate a spot on sample under investigation. The scattered radiations produced by the Raman effect contain information about energies of molecular vibrations and rotations and these depends on particular atoms or ions that comprise the molecule, chemical bonds connect them. During irradiation, the spectrum of the scattered radiation is measured at some angle (often 90 degree) with a suitable spectrometer. Those emitted radiation fall into three categories,

- Stokes scattering
- Anti-stokes scattering
- Rayleigh scattering

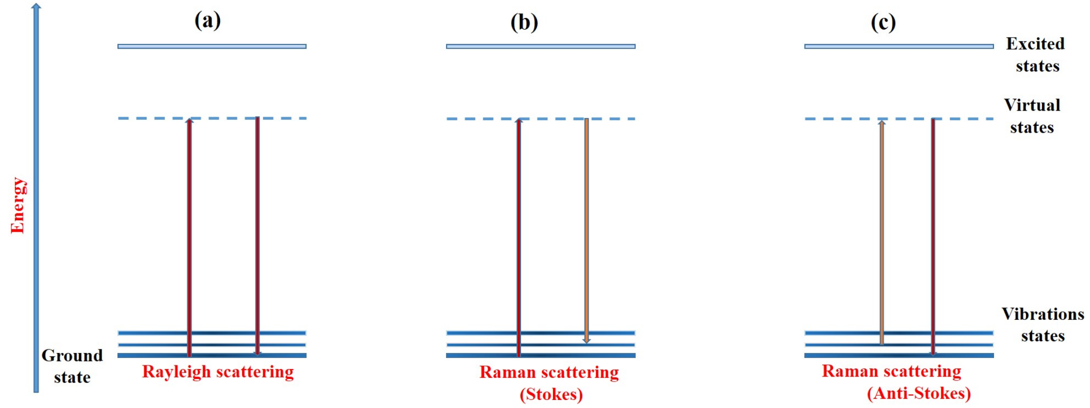

Figure 4.2: Schematic illustration of (a) Rayleigh (b) Stokes (c) anti-Stokes Raman scattering

Reproduced [103]

Raman spectrum comprises of intensity axis (photon counts) against Raman shift (cm^{-1}). Raman shift indicates energy (or frequency) difference value between incident photon and scattered photon. We used Raman spectroscopy at UNAM under ambient environment using 50X objective and 532 nm laser light to collect Raman spectra for 2H-TaS_2, 3R-NbS_2, 1T-$TaTe_2$, 1T-$NbTe_2$ and V_2O_3 ultrathin flakes to confirm their chemical identity and our spectrum matched perfectly with the literature as shown below respectively.

In below figure we have shown Raman spectra that we collected for each material. Raman modes labelled with dashed lines matching with literature for 2H-TaS_2 [104], 1T-$TaTe_2$, 1T-$NbTe_2$ [105] and 3R-NbS_2 [106]. As mentioned in third chapter we did CVD growth of NbS_2 and its Raman spectrum is similar to 3R-NbS_2 spectrum reported in the literature.

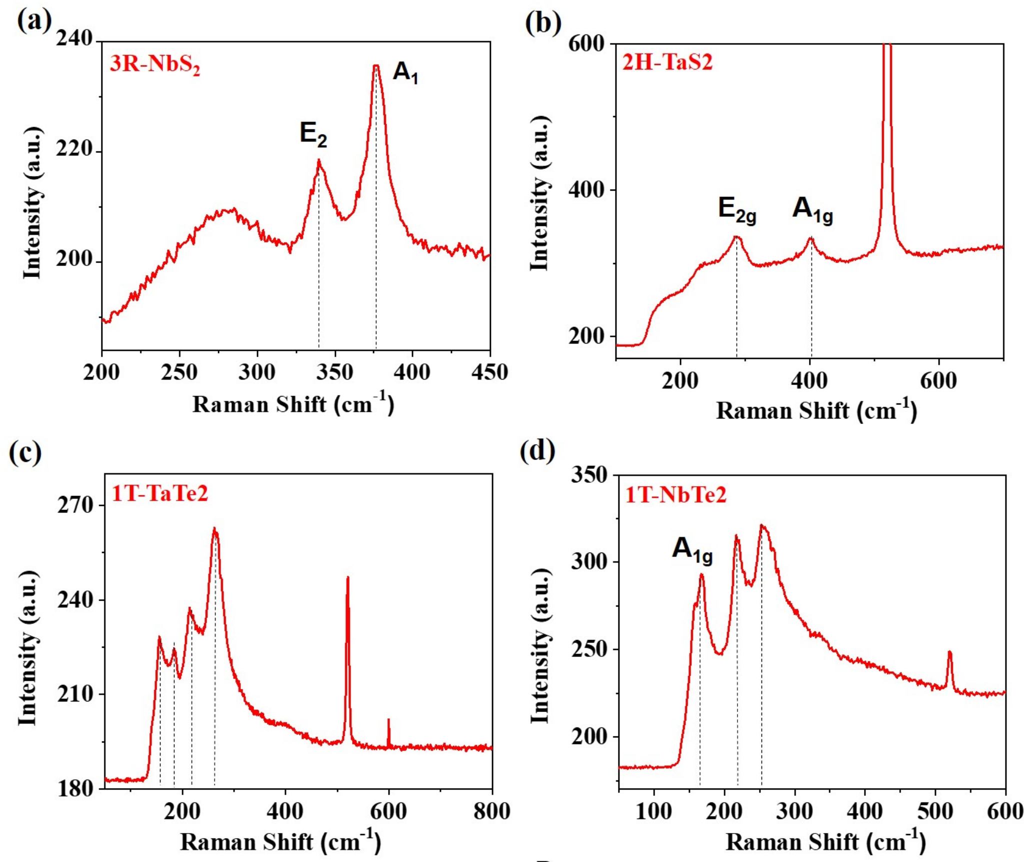

Figure 4.3: Raman profiles of metallic (a) 3R-NbS_2 (b) 2H-TaS_2 (c) 1T-$TaTe_2$ (d) 1T-$NbTe_2$ ultrathin flakes

Below we showed Raman profiles of V_2O_3 insulating (as grow on sapphire) and metallic phases (after transferring on silicon dioxide substrate) with dashed lines indicating the modes matching with literature. These Raman profiles indicate the phases shown in phases stability diagram shown in second chapter.

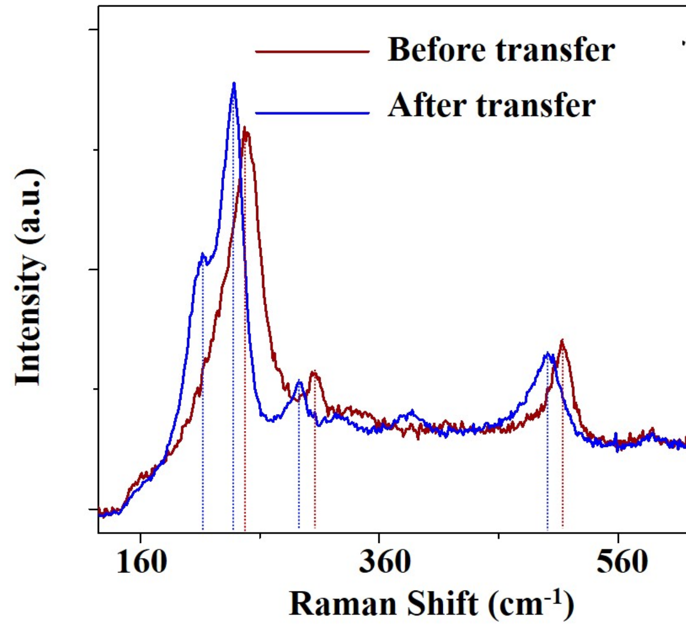

Figure 4.4: Raman profiles of V_2O_3 phases
Reproduced with Copyright Phys. Rev. B (2019)

4.2 Atomic Force Microscopy (AFM) Experiments

KPFM and nano-indentation experiments on atomically ultrathin materials were performed using MFP-3D Asylum AFM. Detailed explanation of both experiments and comprehensive results analysis is illustrated below.

4.2.1 Measurement of Work Function of V_2O_3 using KPFM

Prior to work function calculation of V_2O_3 flakes one should need calibration of AFM probes, for that we followed previously mentioned sample preparation technique. We proposed implementation of an alternative route for work function calibration of AFM tip for KPFM measurement using PECS evaporated (PE) Au on SiO_2 surface as reference material with well known work function value. We opted this method instead of often used material highly oriented pyrolytic graphite (HOPG).

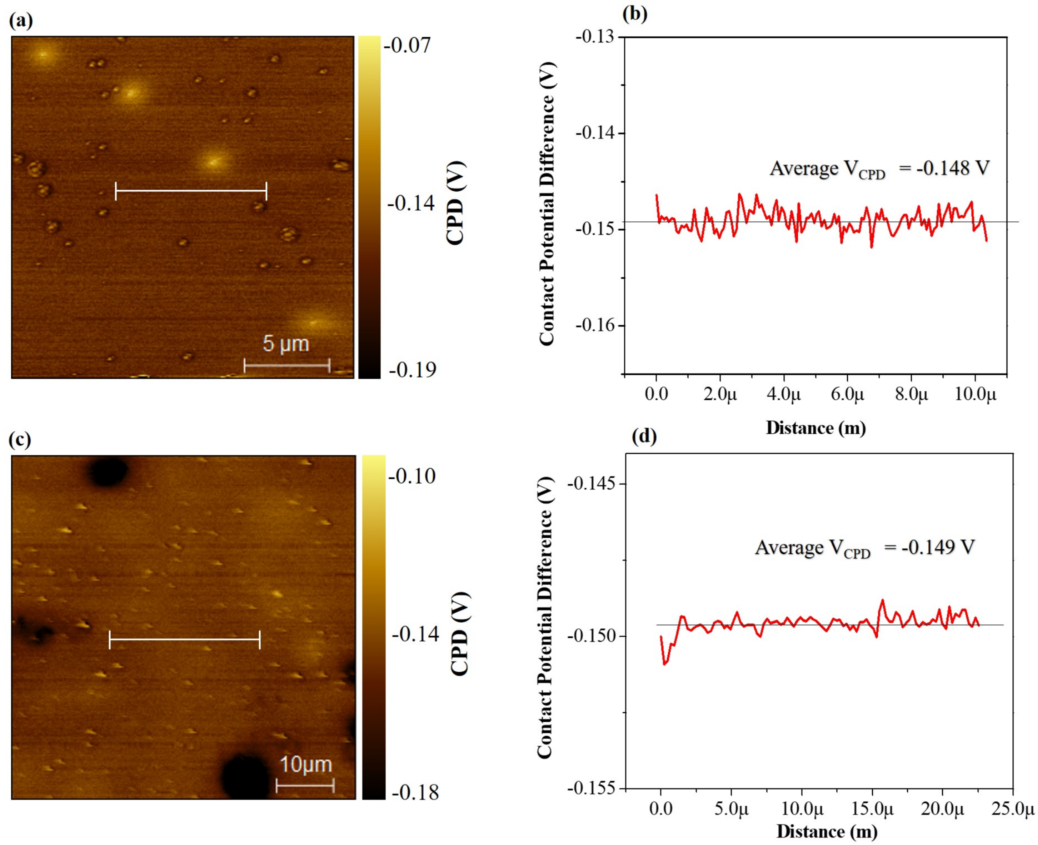

Figure 4.5: CPD maps [(a) and (c)] and CPD profile distribution measured from CPD maps of Au surface [(b) and (d)]

Implementation and usage of this developed protocol gives acquisition of correct and reproducible values of work functions as depicted below (two different Au surfaces are shown with almost same CPD values) and shows some particles and sign of contamination which may come from environment and during sample preparation.

In used protocol, as mentioned in detail in second chapter compensation bias voltages value was applied to probe and resultantly work function of probe was calculated as KPFM produces a CPD and expressed as,

$$V_{cpd} = (\phi_{tip} - \phi_{sample})/e \tag{4.1}$$

$$\phi_{tip} = eV_{cpd} + \phi_{sample} \tag{4.2}$$

Using profile of CPD variation on surface of Au we got average CPD value -0.148 V and used this value and literature defined Au's work function value (5.1) [107] to calculate work function of AFM probe using above relation and found probe's work function as 4.95 eV.

Then considering calibrated work function values of Au (4.95 eV) we calculated work function for atomically thin V_2O_3 flakes using CPD values of it. We again used same sample preparation technique and dual-pas KPFM mode as mentioned in previous chapters to map CPD of V_2O_3 flakes and found it around 4.91 eV.

Below we have optical image of device and first pass AFM topographical image with height profiles shown in third image.

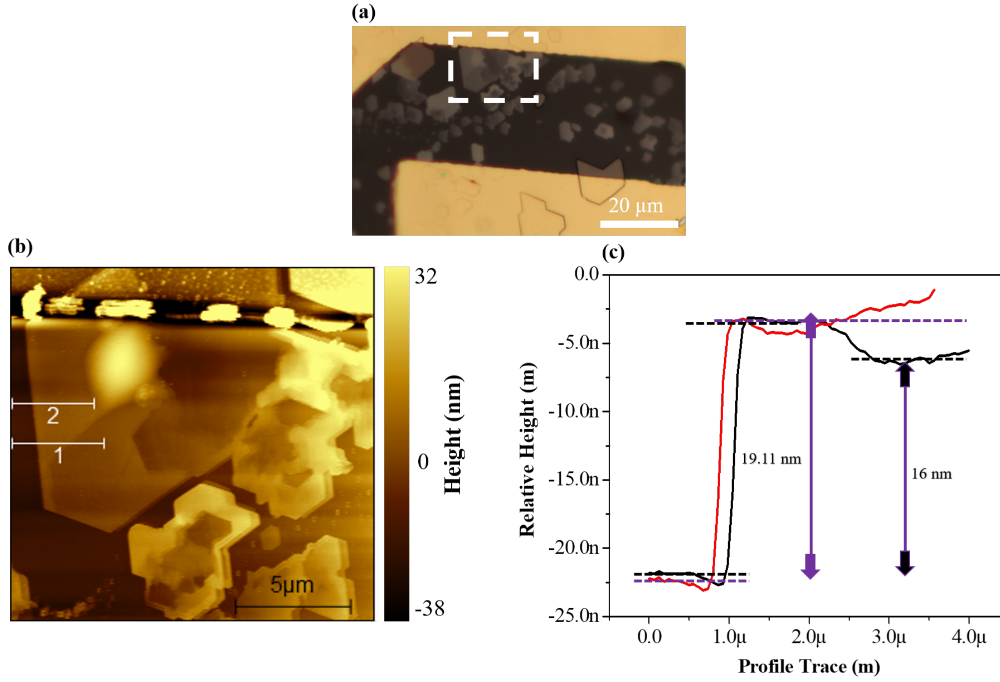

Figure 4.6: (a) Optical image of V_2O_3 flake with Au contact and silver epoxy connection (b) AFM topographical image (c) AFM height profiles from previous image

After topographical image and profiles here we have shown second pass CPD map of V_2O_3 flake with CPD profiles. CPD profiles showing almost no variation in surface potential taken from different places (different height regions as shown in previous image). Average CPD value we found from the map is 0.04 V and calibrated work function of AFM probe 4.95 eV we used below formula to calculate work function for V_2O_3 flake which came 4.91 eV.

$$\phi_{sample} = \phi_{tip} - eV_{cpd} \tag{4.3}$$

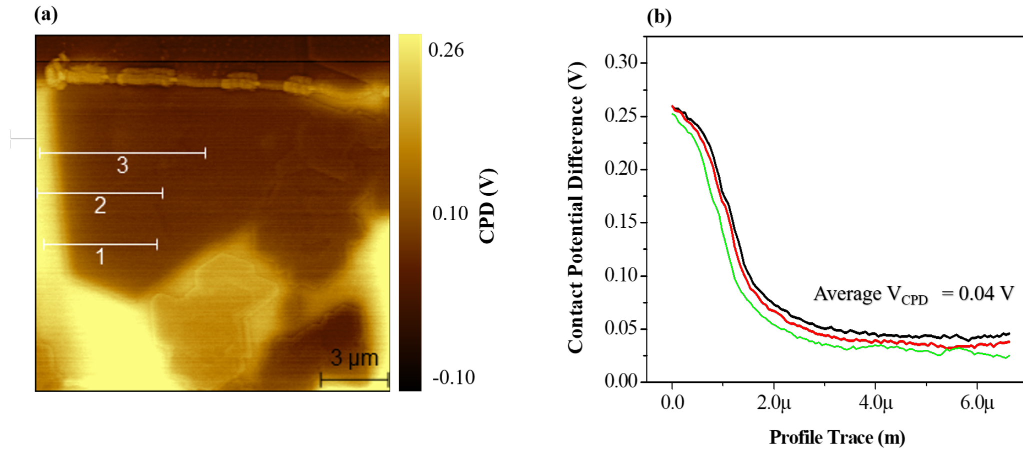

Figure 4.7: (a) CPD map of V_2O_3 flake (b) CPD profiles from previous different region in image

There might be small error margin in work function values of V_2O_3 as we performed KPFM experiments in ambient. And we have literature evidences about performing KPFM in ambient may influenced by humidity, surface dipole layer, static surface charges, water layer adsorption and unavoidable contamination and all these factors tend to effect resolution and surface potential profile [108] [109] [110].

4.2.2 Measurement of Mechanical Properties of Various Ultrathin 2D Materials via F-D Curves

During mechanical nanoindentation tests, a point force is applied on suspended flake while simultaneously subsequent deformation is noted. Assessment of mechanical features of atomically thin TMDCs flakes comprises of nano-indentation testing, data analysis through MATLAB and origin Lab software. Brief description is as follow,

4.2.2.1 Nanoindentation Testing

The technique to do nanomechanical characterization through AFM nanoindentation obey force-distance manner fitted through least square method explained in detail in second chapter. First, we performed hard strike on SiO_2 substrate using AFM contact mode to get lever sensitivity (InvOLS) which later on we used to calculate spring constant of AFM cantilever. All the steps of calibration and relevant significant information is briefly mentioned in chapter 3. using thermal method, calibration of AFM probes gave us spring constant value perfectly in the range of provided by sellers.

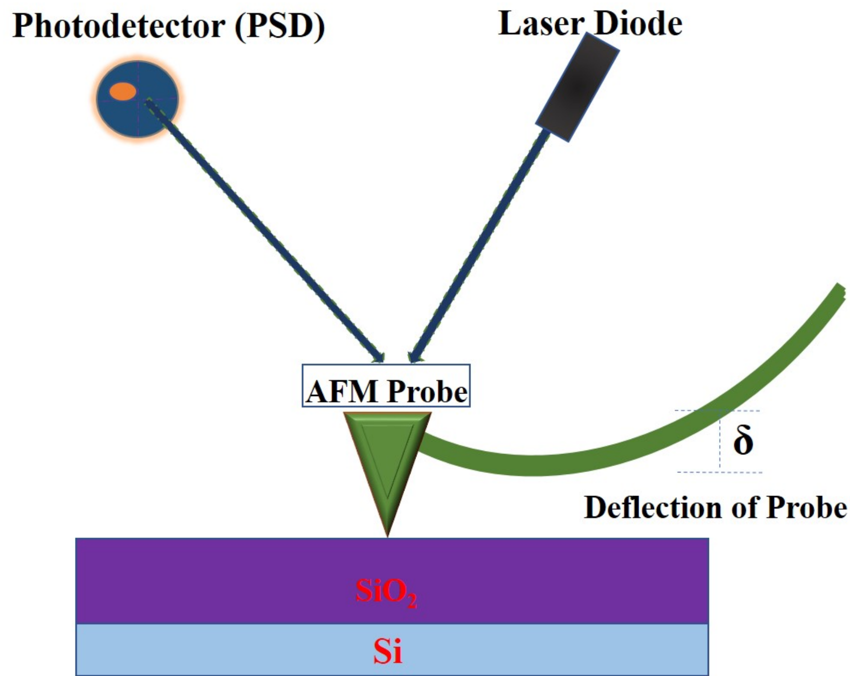

Figure 4.8: (a) AFM probe striking against SiO_2

4.2.2.2 Analysis of Elastic Modulus and Pretension in Suspended 2D Flakes

After doing sensitive calibration of AFM probe and finding related spring constant via thermal tunning technique, we placed our sample for measurement.

Sample preparation is briefly explained in chapter 3, here some of related images (optical image, AC mode AFM topographical image with related height profiles) are placed.

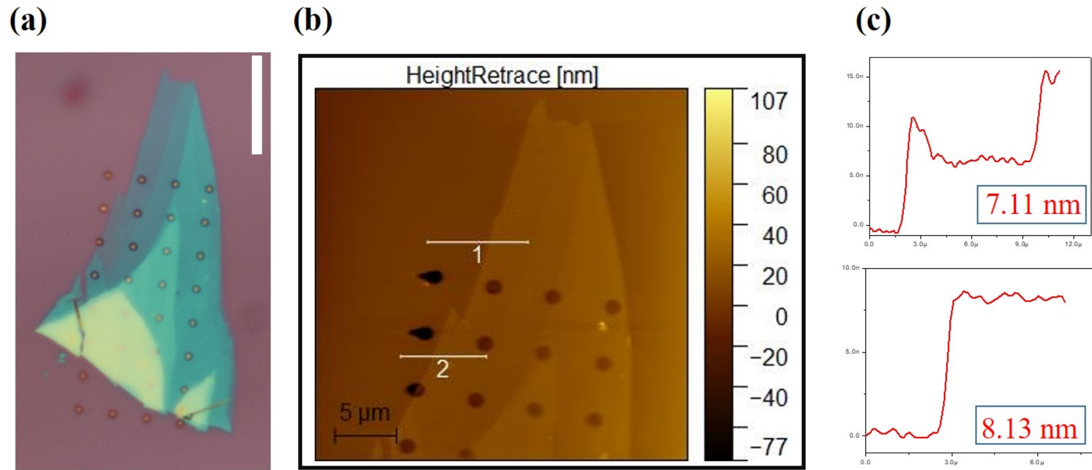

Figure 4.9: (a) 2H-TaS_2 optical image with scale bar 10 μm (b) related topography (c) height profiles

We performed series of nano-indentation experiments on 2H-TaS_2, 3R-NbS_2, 1T-$TaTe_2$ and 1T-$NbTe_2$ having different thicknesses. After setting our sample we traced the topography using tapping mode as shown in picture above, after we chose suitable hole region without any crack and wrinkle and scanned it unless we got thermal drift free image as shown below. We applied steadily increasing force upto breaking point of the 2D flakes.

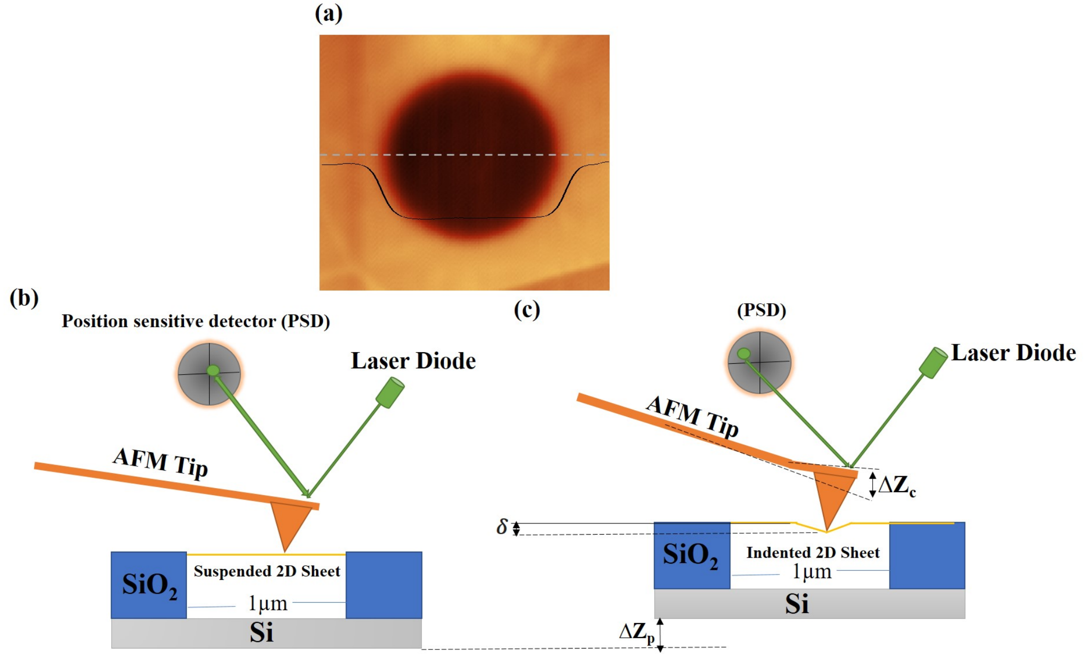

Figure 4.10: (a) 2H-TaS_2 flake zoomed-in topographic image suspended over hole showing strong clamped behaviour (b) schematic before and (c) after indentation

Deflection of the suspended sheet was estimated using this calculation,

$$\delta = \Delta Z_p - \Delta Z_c \tag{4.4}$$

Then using obtained deflection and spring constant values, we estimated E^{2D} and σ_0^{2D} by least square fitting of below equation to related force-indentation curves.

$$F = \frac{4\pi E t^3}{3(1-v^2)R^2}\delta + (\sigma_0^{2D}\pi)\delta + [E^{2D}\frac{q^3}{R^2}]\delta^3 \tag{4.5}$$

As most of our suspended flakes of 2H-TaS_2 were ultrathin and thickness is much less compare to radius of FIB drilled holes. Therefore, bending rigidity term became invalid so expression comprises of stretching of flake along with non-linear stiffness will be taken into consideration,

$$F = (\sigma_0^{2D}\pi)\delta + [E^{2D}\frac{q^3}{R^2}]\delta^3 \tag{4.6}$$

Comprehensive explanation of this model is illustrated in literature review part chapter 2. Before evaluating and data processing using above mentioned equation, for correct force-indentation curves it is crucial to finalize zero displacement

and force point (ZDP) accurately. At this point, applied force and resulted displacement both are zero. During nanoindentation tests, AFM probe remained fixed after placing into holder, while sample on XY piezoelectric scanner plate moves towards tip. We chose origin, after extrapolating linear force-indentation dependence way before contact of tip and sample until this line crosses curved region and defined this point as ZDP [111]. It is highly crucial to determine ZDP for indentation tests as 2-5 nm deviation or inaccuracy from exact ZDP lead 20 % error in resulted in-plane modulus (E^{2D}) [95]. We used Poisson's ratio 0.27 (defined in literature) for 2H-TaS_2 and 500 nm radius of the hole for our nanoindentation tests.

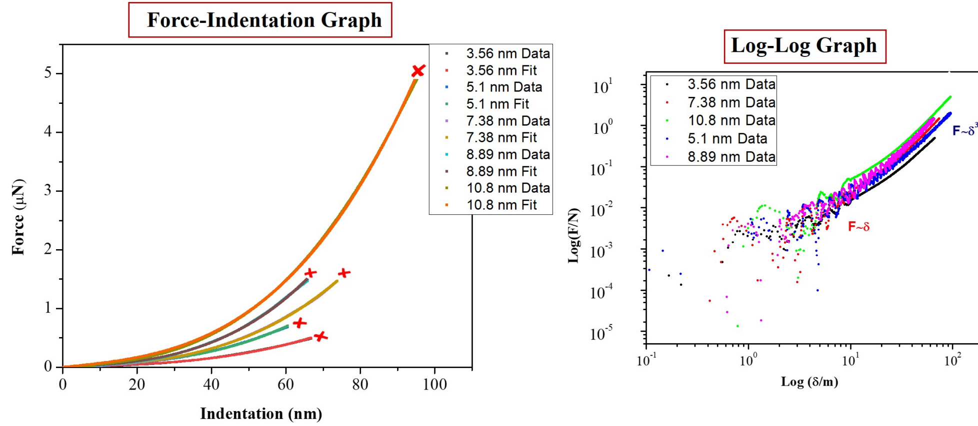

Figure 4.11: (a) Force versus indentation of 2H-TaS_2 sheets with fitting (red crosses show breaking point of sheets that gives breaking stress) (b) log graph showing liner and cubic region at lower and higher loads respectively

To validate nanoindentation test with contact model above figure illustrates main 5 representative indentation curves for 2H-TaS_2 acquired with thickness range as 3.56 - 10.80 nm. All our experimental data agreed well with the related fitted curves (fitting parameter R^2 Value is around 0.998 for all curves) demonstrate perfect reliability of mechanical model and valid data analysis. Using this model, curves show linear path and less deformation under lower force values while notably follows cubic trend when force gets larger. [Also explained through log-log graph]

For 2H-TaS_2, we used ramping mode (Force vs Deflection) of AFM and indented around 30 thin suspended sheets having different thickness values to acquire a reasonable estimation of mechanical characteristics. Corresponding in-plane elastic modulus and pretension values were obtained using contact model equation. To compare our findings with other TMDCs we converted these in-plane values to volumetric/conventional (3D) values. We achieved this, by dividing them against thickness of observed flakes [22].

First, we analyzed pretension (σ_o^{2D}) in N/m and prestress (σ_o^{3D}) in GPa (by dividing pretension against thickness) in 2H-TaS_2 suspended flakes using continuum mechanics formula mentioned above. Major contribution in the assessment of these values, comes from second term in the formula. Pretension σ_o^{2D} is independent against thickness and values range between 0.5-2.5 N/m. σ_o^{2D} graph depicts no relation between measured values and thickness. Also, prestress graph is shown in fig (b).

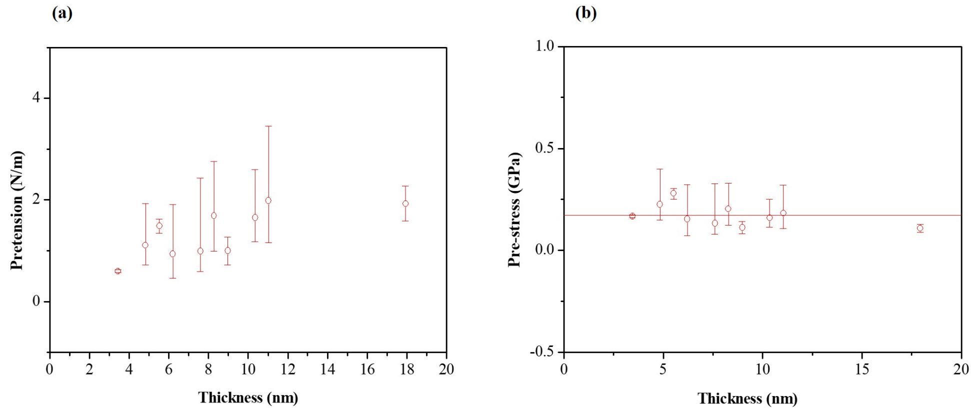

Figure 4.12: (a) 2D pretension (b) prestress of $2H - TaS_2$ flakes

Also, prestress arises from mechanical exfoliation and PDMS stamp transfer technique. During this procedure, when PDMS and 2D flakes press together it results lateral expansion of PDMS stamp (because of its softness) [112] that will stretch 2D flakes upto certain extent. While upon peeling PDMS stamp off lead to induce some positive pretension in 2D flakes which were already stretched and adhere to SiO_2 surface through van der Waals forces. Moreover, pretension in

flakes can be decreased using vacuum annealing method [113].

Secondly, we measured in-plane (E^{2D}) and volumetric elastic/Young's modulus (E^{3D}) of 2H-TaS_2 suspended flakes having different thickness range, and we found in-plane modulus increases linearly versus thickness while volumetric modulus shows thickness independence like other TMDCs reported in literature so far.

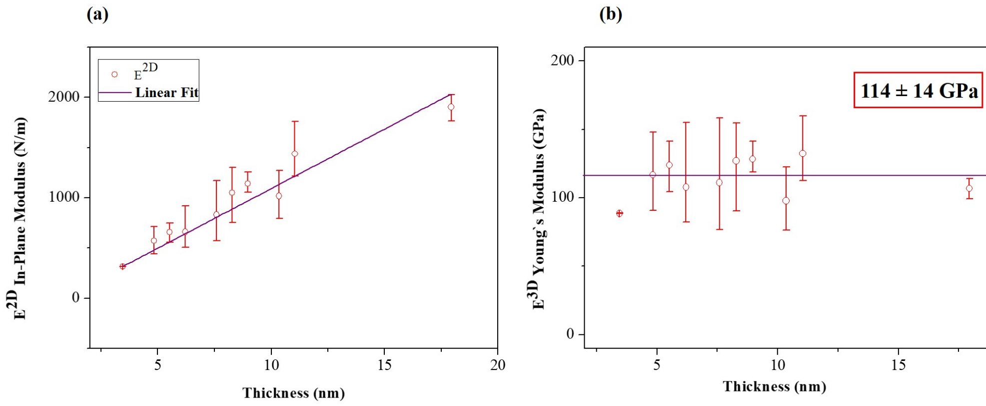

Figure 4.13: Elastic properties of 2H-TaS_2 flakes: (a) In-plane modulus (b) bulk Young's modulus against thickness

If E^{3D} of a material shows no dependency on thickness, then E^{2D} should manifest linearly increasing trend versus thickness of flake [23] [114] and we have same trend in our E^{2D}/E^{3D} values. We found interlayer sliding (coming from van der Waals forces between flake and substrate) causes to soften resulted modulus for layered materials [22]. Because of this interlayer sliding effect, E^{3D} value would decrease as thickness increased.

But our results like other TMDCs provide an indication of interlayer sliding saturation that causes Young's modulus to be independent of layer thickness like other 2D materials [21][22][23][75]. Also, our suspended flakes are clamped tightly with edges of FIB drilled holes indicates no sliding on substrate that suppresses interlayer sliding too. We summarized E^{3D} values for suspended 2H-TaS_2 flakes with different thickness and average Young's modulus value is 114$\pm$14 and this value is slightly lower when comparing with measured semiconductor TMDCs.

4.2.2.3 Tensile or Breaking Strength

To enable commercial applications of our suspended materials in strain based and flexible electronics, we determined maximum breaking strength under force. As mentioned in previous sections, breaking strength of 2D flakes can be investigated by increasing applied force untill mechanical failure (fracture or rupture) occurs. Our nano-indentation tests lies in the limit of small indenter defined through $\frac{r_{tip}}{r}$<1(0.018 for our case) and using concept of linear elastic membrane theory maximum stress applied at center of suspended flake can be totalized by:

$$\sigma_m^{2D} = \sqrt{\frac{F_{max}E^{2D}}{4\pi R_{tip}}} \tag{4.7}$$

We extracted maximum strength pointed at central region of suspending 2D sheets utilizing above expression for linearly elastic circular flake under sharp spherical indenter as applied force reaches to breaking point suspended flake collapses that indicates mechanical failure. Fracture of our suspended flakes occurred in the middle of suspending region (as shown in picture) where AFM probe applied maximum loading force (around 1100 nN) instead of edge of suspended material. Also, we showed complete steps of AFM tip and suspended flakes.

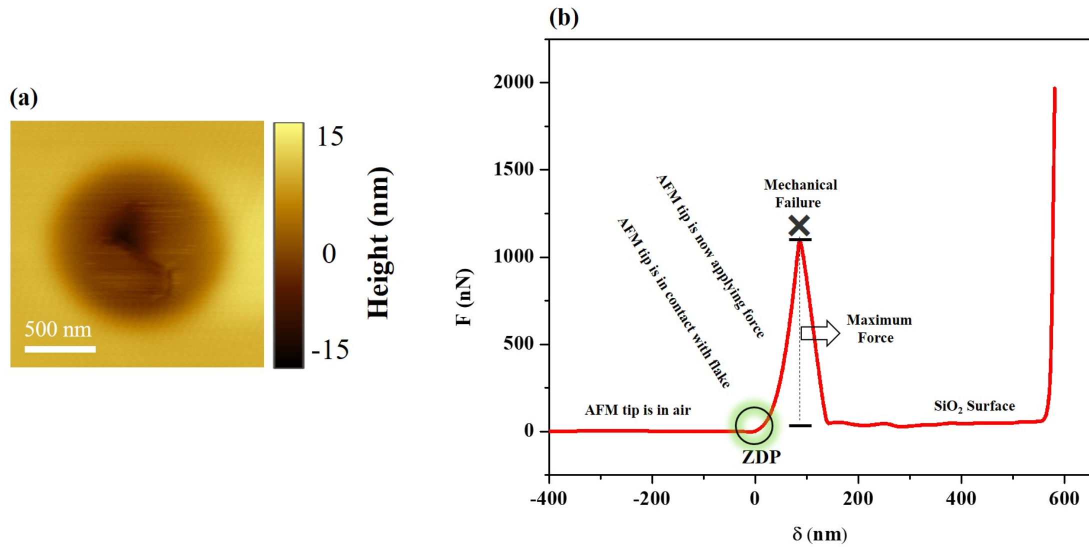

Figure 4.14: (a) AFM image of 2H-TaS_2 flake after fracture in center (b) F-D curve steps explanation

As radius of AFM tip is dominant contributor towards calculation of breaking stress and strength. In our studies, we used Tap300Al-g AFM probes with spring constant 40 N/m and radius 10 nm reported by manufacturer. But way before nano-indentation we performed hard strike of AFM probes on SiO_2 surface to calibrate deflection sensitivity and scanned dummy sample to minimize thermal drift of AFM piezo actuators. These two steps may degrade the tip radius and increase it from 10 nm to unknown values. So, keeping importance of radius of tip in our consideration, we took high resolution SEM images of AFM probes before and after nano-indentation tests to know about wear and degradation of tip radius as shown below.

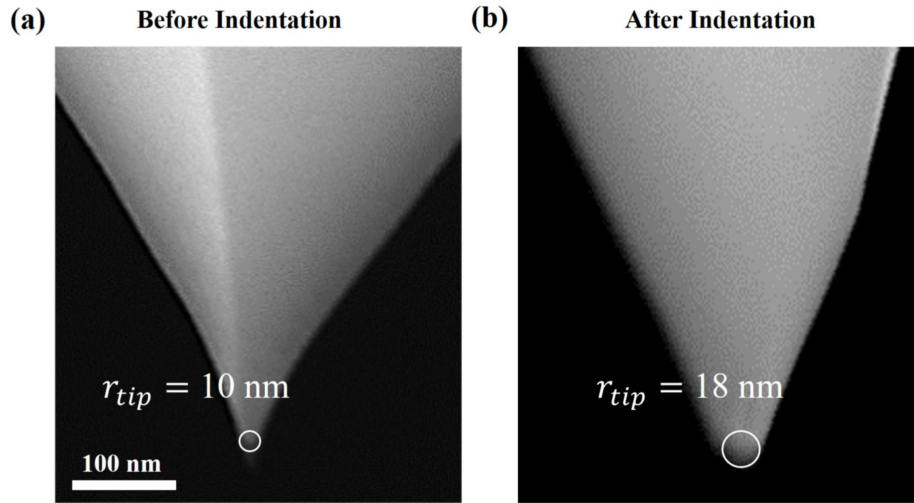

Figure 4.15: (a) Before indentation pristine tip radius 10 nm (b) after indentation image shows broadening in radius

Through high resolution SEM images, we found significant degradation and broadening of radius from 10 nm to 18±2 nm. This much broadening renders maximum 2D breaking stress between 50 and 350 N/m against increasing thickness values. This 2D finding lead us to calculate 3D breaking strength just by diving in-pane breaking strength by the thickness of corresponding 2D flakes [σ_m^{3D}=(σ_m^{2D})/(thickness)] and both results are depicted below.

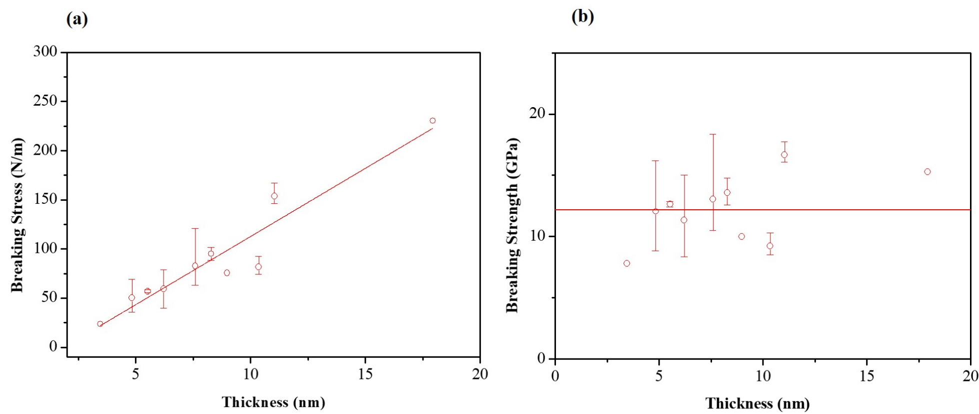

Figure 4.16: (a) Before indentation pristine tip radius 10 nm (b) after indentation image shows broadening in radius

2D breaking stress follows linearly increasing trend versus thickness of flake same like in-plane modulus whereas breaking strength is thickness independent and average value is 12.6 ± 2.6 GPa which is 11% of bulk modulus. This 11% means, 11% maximum strain value when considering stress-strain linear relationship given below.

$$\sigma = E^{3D}\epsilon \tag{4.8}$$

We also measured other metallic TMDCs ultrathin flakes (shown below) to compare their elastic responses under nano-indentation testing.

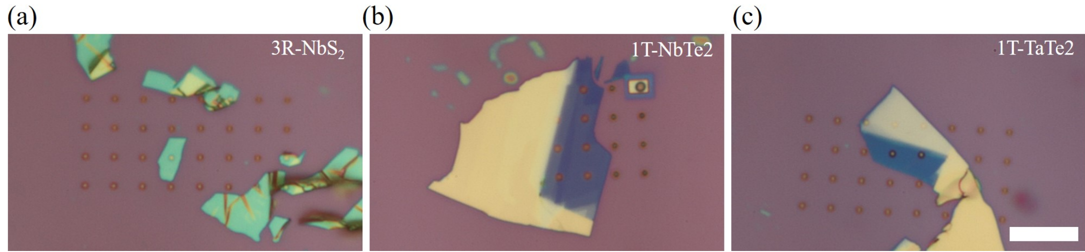

Figure 4.17: Optical microscope images of (a) 3R-NbS_2 (b) 1T-$NbTe_2$ (c) 1T-$TaTe_2$ ultrathin flakes (Scale bar is 10 μm)

Same methodology and AFM tips were used to indent these metallic TMDCs's flakes as well. We measured number of samples for each material to verify the confirm mechanical properties. Same like 2H-TaS_2 we recorded their elastic response using continuum model mechanics. Only difference comes in Poisson's ratio of materials which we took from literature and verified them using ab-initio calculations. Poisson's ratio values used for these metallic TMDCs are as: 2H-TaS_2 0.27 3R-NbS_2 0.27, 1T-$NbTe_2$ 0.11 and 1T-$TaTe_2$ 0.10 [115]. Below we have shown comparison of mechanical features of all four metallic materials.

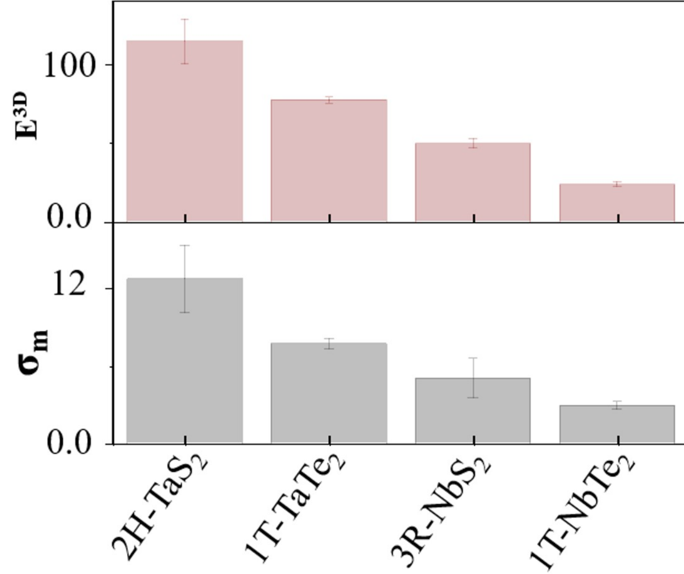

Figure 4.18: Comparison of Young's modulus and breaking strength of metallic TMDCs's

Above we compared Young's modulus and breaking strength of the metallic TMDCs. Breaking strength was calculated using 4.7 equation as a function of applied load force and particularly radius of AFM tip and using equation 4.8 we calculated nominal strain % values as shown in table 4.1. But this formalism is coming from linear mechanics and we considered suspended material is in linear stress-strain regime. Whereas Lee *et al.*, stated elastic response of suspended sheets must be in non-linear regime as magnitude of strain under AFM tip is reasonably high that indicates consideration of non-linear regime for calculation of intrinsic breaking strength [8]. To calculate intrinsic breaking strength (ultimate strain) at breaking force, stress-strain response of metallic TMDCs can be consider as large area isotropic membrane under effect of uniaxial stress (as local stress mainly concentrated in the area right under indenter tip) and can be written as

$$\sigma = E\epsilon + D\epsilon^2 \tag{4.9}$$

where σ known as second Piola-Kirchhoff stress value, ϵ is Lagrangian strain and D is 3rd order elastic modulus [8]. Using maximum breaking strength response

one can calculate D, as

$$D = -\frac{E^2}{4\sigma_m} \tag{4.10}$$

Then using relationship of D, ultimate intrinsic strain is,

$$\epsilon_m = -\frac{E}{2D} \tag{4.11}$$

Now after plugging in the values of D (calculated from breaking strength response) and E (calculated from in-plane modulus of F-D curve) we measured ultimate strain for metallic TMDCs. 2H-TaS_2, 1T-$TaTe_2$, 3R-NbS_2 and 1T-$NbTe_2$ showed 0.22, 0.21, 0.20 and 0.25 respectively which are higher than all reported 2D materials and comparable to graphene (0.25). These comprehensive calculation of ultimate strain values provide an insight into ultimate strength of a material, for example intrinsic strength's theoretical limit for brittle materials is $\sigma_m \approx E^{3D}/9$. And we calculated ratio of Young's modulus to breaking strength for all four materials is approximately 8.

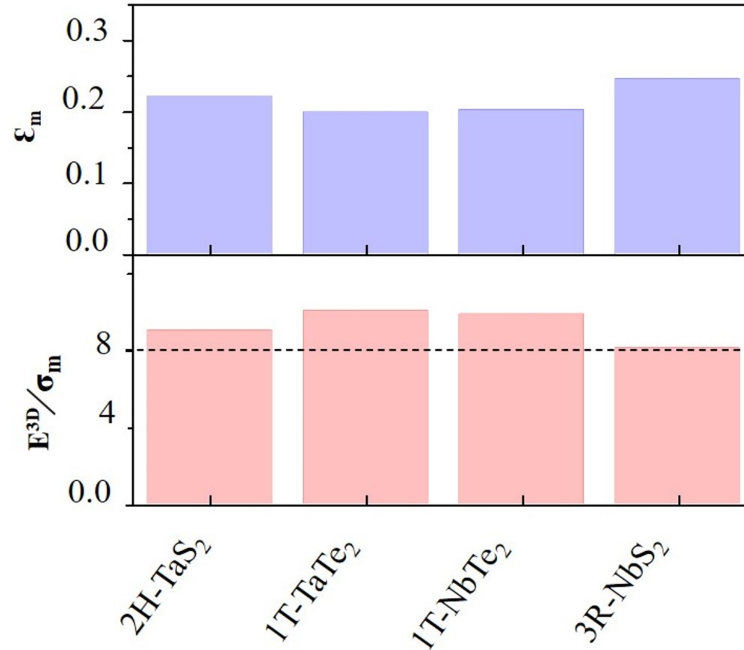

Figure 4.19: Comparison of ultimate strain values and ratio of E^{3D} to breaking strength of metallic TMDCs's

Below in table we showed comparison between elastic features of 2D materials reported so far and measured in this study. Our metallic TMDCs showed relatively lower Young's modulus than most of the materials in literature but surprisingly maximum nominal strain (calculated by assuming stress and strain linear relationship, σ=Eϵ) values for our materials are significantly higher than all materials and comparable to graphene. This much nominal strain values superior to mostly aforementioned results are an indication that ultrathin metallic TMDCs are convenient to use in future flexible electronics devices.

	Material	**E^{3D} (GPa)**	**σ_m (GPa)**	**Strain (%)**	**References**
1	Graphene (monolayer)	1000±100	130	13	[8]
2	$NbTe_2$ (multilayer)	23.6±1.6	2.9±0.3	12	This Work
3	TaS_2 (multilayer)	114±14	12.6±2.6	11	This work
4	$TaTe_2$ (multilayer)	69±7	7.2	10	This work
5	NbS_2 (multilayer)	49.4±3	5.0	10	This Work
6	hBN (1-9 layers)	861±4	72±4	8	[114]
7	MoS_2 (monolayer)	270±100	22±4	8	[75]
8	WS_2 (monolayer)	272	N/A	N/A	[22]
9	WSe_2 (multilayer)	167±6.7	12.4	7.3	[23]
10	GaTe (10 nm)	24.6±16	2	7	[88]
11	$Ti_3C_2T_x$ (monolayer)	333±30	17.3±1.6	5.1	[111]
12	GaSe (10 nm)	81.9±12.7	4	5	[88]
13	GaS (10 nm)	173±15	8	4.5	[88]

Table 4.1: Table 1 summarizes comparison of elastic properties of 2D materials

Chapter 5

Conclusion and Future Work

To summarize our work, we demonstrated KPFM and Nano-indentation experiments on ultrathin materials using Asylum AFM. Using dual pass KPFM mode, we first measured the CPD map between Au coated tip and Au surface and used this map to calibrate work function of tip that came 4.95 eV matches nearly with literature. Then by using this calibrated tip we measured CPD map between tip and CVD grown V_2O_3 flakes and found work function 4.91 eV for V_2O_3 first time which may have small error margin as we performed KPFM measurements in ambient. This Knowledge of work function values will help in electrical device performance and will provide essential concept to chose appropriate metal electrode contacts with closer work function value to V_2O_3.

As mechanical characteristics of 2D ultrathin membranes got numerous attention recently. So, by using nano-indentation we indented PDMS based exfoliated metallic TMDCs suspending over FIB drilled holes upto their mechanical failure to check their modulus, strength and stability under stress and applied force. For this purpose, we experimentally indented metallic suspended flakes with different thickness especially wide range of indentation experiments were done on 2H-TaS_2. For metallic TMDCs, we found linearly increasing in-plane modulus against thickness while Young's modulus found to be completely thickness independent. This thickness independent behaviour indicates saturation of interlayer

sliding, this sliding causes modulus to change with thickness. The Young's modulus for multilayer metallic TMDCs is as: 2H-TaS_2 is 114±14 GPa, 1T-$TaTe_2$ is 70 ± 14 GPa, 3R-NbS_2 is 49.4 ± 3 GPa and lastly 1T-$NbTe_2$ is 23.6±1.6 GPa. Our obtained Young's modulus values for metallic TMDCs are relatively lower as compare to reported values for semiconducting TMDCs. Other than Young's modulus, we analyzed breaking strength, ultimate/breaking strain values (which are greater than all 2D materials except graphene) of these materials as well. Fracture failure tests revealed that metallic 2H-TaS_2, 1T-$TaTe_2$, 3R-NbS_2 and 1T-$NbTe_2$ can withstand 12.6±2.6 GPa, 7.18±0.40 GPa, 5.0±1.5 GPa and 2.9±0.3 stress respectively and corresponding to 11%, 10 %, 10% and 12 % respectively maximum strain before breaking. Also, we found intrinsic strain values considering stress-strain relationship in non-linear regime because of high strain magnitude right under sharp AFM tip and values for intrinsic strain are as, 2H-TaS_2 0.22, 1T-$TaTe_2$ 0.21, 3R-NbS_2 0.20 and 1T-$NbTe_2$ 0.25. These linearly and nonlinearly measured strain values for metallic TMDCs are way larger than semiconducting TMDCs and comparable to graphene which makes them favorable contestants for flexible electronics, nanoscale devices especially as a contact materials with other TMDCs.

As elasticity is considered as basic mechanical hallmark of 2D materials and it is pivotal for their usage in commercial strain engineering applications. And mechanical properties are essential determinants for strain-induced engineering of 2D materials and play vital roles in designing of 2D flexible devices [21][116][117]. Strain engineering proved to be promising mechanism to modulate electronic and optical properties [118], materials we analyzed they can be use in strain-induced based devices, piezoresistive/piezoelectric devices and in nanoelectromechanical systems (NEMSs) because of their extraordinary metallic features measured.

Bibliography

[1] R. P. Feynman, "There's plenty of room at the bottom," *California Institute of Technology, Engineering and Science magazine*, 1960.

[2] K. S. Novoselov, A. K. Geim, S. V. Morozov, D. Jiang, Y. Zhang, S. V. Dubonos, I. V. Grigorieva, and A. A. Firsov, "Electric field effect in atomically thin carbon films," *science*, vol. 306, no. 5696, pp. 666–669, 2004.

[3] M. Dresselhaus and G. Dresselhaus, "Intercalation compounds of graphite," *Advances in Physics*, vol. 30, no. 2, pp. 139–326, 1981.

[4] N. D. Mermin, "Crystalline order in two dimensions," *Physical Review*, vol. 176, no. 1, p. 250, 1968.

[5] V. Singh, D. Joung, L. Zhai, S. Das, S. I. Khondaker, and S. Seal, "Graphene based materials: past, present and future," *Progress in materials science*, vol. 56, no. 8, pp. 1178–1271, 2011.

[6] M. Batzill, "The surface science of graphene: Metal interfaces, cvd synthesis, nanoribbons, chemical modifications, and defects," *Surface Science Reports*, vol. 67, no. 3-4, pp. 83–115, 2012.

[7] Y. Wu, X. Ruan, C.-H. Chen, Y. J. Shin, Y. Lee, J. Niu, J. Liu, Y. Chen, K.-L. Yang, X. Zhang, *et al.*, "Graphene/liquid crystal based terahertz phase shifters," *Optics express*, vol. 21, no. 18, pp. 21395–21402, 2013.

[8] C. Lee, X. Wei, J. W. Kysar, and J. Hone, "Measurement of the elastic properties and intrinsic strength of monolayer graphene," *science*, vol. 321, no. 5887, pp. 385–388, 2008.

[9] Q.-X. Pei, Z.-D. Sha, and Y.-W. Zhang, "A theoretical analysis of the thermal conductivity of hydrogenated graphene," *Carbon*, vol. 49, no. 14, pp. 4752–4759, 2011.

[10] E. P. Randviir, D. A. Brownson, and C. E. Banks, "A decade of graphene research: production, applications and outlook," *Materials Today*, vol. 17, no. 9, pp. 426–432, 2014.

[11] Y.-M. Chen, S.-M. He, C.-H. Huang, C.-C. Huang, W.-P. Shih, C.-L. Chu, J. Kong, J. Li, and C.-Y. Su, "Ultra-large suspended graphene as a highly elastic membrane for capacitive pressure sensors," *Nanoscale*, vol. 8, no. 6, pp. 3555–3564, 2016.

[12] A. Castellanos-Gomez, M. Poot, G. A. Steele, H. S. Van Der Zant, N. Agraït, and G. Rubio-Bollinger, "Elastic properties of freely suspended mos2 nanosheets," *Advanced Materials*, vol. 24, no. 6, pp. 772–775, 2012.

[13] B. Radisavljevic, A. Radenovic, J. Brivio, V. Giacometti, and A. Kis, "Single-layer mos 2 transistors," *Nature nanotechnology*, vol. 6, no. 3, p. 147, 2011.

[14] K. Chen, X. Wan, and J. Xu, "Epitaxial stitching and stacking growth of atomically thin transition-metal dichalcogenides (tmdcs) heterojunctions," *Advanced Functional Materials*, vol. 27, no. 19, p. 1603884, 2017.

[15] R. Lv, J. A. Robinson, R. E. Schaak, D. Sun, Y. Sun, T. E. Mallouk, and M. Terrones, "Transition metal dichalcogenides and beyond: synthesis, properties, and applications of single-and few-layer nanosheets," *Accounts of chemical research*, vol. 48, no. 1, pp. 56–64, 2014.

[16] M. R. Habib, W. Chen, W.-Y. Yin, H. Su, and M. Xu, "Simulation of transition metal dichalcogenides," in *Two Dimensional Transition Metal Dichalcogenides*, pp. 135–172, Springer, 2019.

[17] N. Mehmood, H. R. Rasouli, O. Çakıroğlu, and T. S. Kasırga, "Photocurrent generation in a metallic transition-metal dichalcogenide," *Physical Review B*, vol. 97, no. 19, p. 195412, 2018.

[18] O. Çakıroğlu, N. Mehmood, M. M. Çiçek, A. Aikebaier, H. R. Rasouli, E. Durgun, and T. S. Kasırga, "Thermal conductivity measurements in nanosheets via bolometric effect," *arXiv preprint arXiv:2001.00368*, 2020.

[19] T. kumar Agarwal, B. Soree, I. Radu, P. Raghavan, G. Iannaccone, G. Fiori, W. Dehaene, and M. Heyns, "Material-device-circuit co-optimization of 2d material based fets for ultra-scaled technology nodes," *Scientific reports*, vol. 7, no. 1, pp. 1–7, 2017.

[20] A. Castellanos-Gomez, M. Poot, A. Amor-Amorós, G. A. Steele, H. S. van der Zant, N. Agraït, and G. Rubio-Bollinger, "Mechanical properties of freely suspended atomically thin dielectric layers of mica," *Nano Research*, vol. 5, no. 8, pp. 550–557, 2012.

[21] Y. Sun, J. Pan, Z. Zhang, K. Zhang, J. Liang, W. Wang, Z. Yuan, Y. Hao, B. Wang, J. Wang, *et al.*, "Elastic properties and fracture behaviors of biaxially deformed, polymorphic mote2," *Nano letters*, vol. 19, no. 2, pp. 761–769, 2019.

[22] K. Liu, Q. Yan, M. Chen, W. Fan, Y. Sun, J. Suh, D. Fu, S. Lee, J. Zhou, S. Tongay, *et al.*, "Elastic properties of chemical-vapor-deposited monolayer mos2, ws2, and their bilayer heterostructures," *Nano letters*, vol. 14, no. 9, pp. 5097–5103, 2014.

[23] R. Zhang, V. Koutsos, and R. Cheung, "Elastic properties of suspended multilayer wse2," *Applied Physics Letters*, vol. 108, no. 4, p. 042104, 2016.

[24] G. Binnig, H. Rohrer, C. Gerber, and E. Weibel, "Surface studies by scanning tunneling microscopy," *Physical review letters*, vol. 49, no. 1, p. 57, 1982.

[25] G. Binnig, C. F. Quate, and C. Gerber, "Atomic force microscope," *Physical review letters*, vol. 56, no. 9, p. 930, 1986.

[26] N. Jalili and K. Laxminarayana, "A review of atomic force microscopy imaging systems: application to molecular metrology and biological sciences," *Mechatronics*, vol. 14, no. 8, pp. 907–945, 2004.

[27] H. Zhang, J. Huang, Y. Wang, R. Liu, X. Huai, J. Jiang, and C. Anfuso, "Atomic force microscopy for two-dimensional materials: A tutorial review," *Optics Communications*, vol. 406, pp. 3–17, 2018.

[28] M. R. Mozafari, C. Reed, C. Rostron, and V. Hasirci, "A review of scanning probe microscopy investigations of liposome-dna complexes," *Journal of liposome research*, vol. 15, no. 1-2, pp. 93–107, 2005.

[29] M. R. P. Ragazzon, "Parameter estimation in atomic force microscopy: Nanomechanical properties and high-speed demodulation," 2018.

[30] Y. F. Dufrêne, T. Ando, R. Garcia, D. Alsteens, D. Martinez-Martin, A. Engel, C. Gerber, and D. J. Müller, "Imaging modes of atomic force microscopy for application in molecular and cell biology," *Nature nanotechnology*, vol. 12, no. 4, p. 295, 2017.

[31] R. W. Stark, G. Schitter, M. Stark, R. Guckenberger, and A. Stemmer, "State-space model of freely vibrating and surface-coupled cantilever dynamics in atomic force microscopy," *Physical Review B*, vol. 69, no. 8, p. 085412, 2004.

[32] R. Garcıa and R. Perez, "Dynamic atomic force microscopy methods," *Surface science reports*, vol. 47, no. 6-8, pp. 197–301, 2002.

[33] F. M. Etzler and J. Drelich, "Atomic force microscopy for characterization of surfaces, particles, and their interactions," in *Developments in Surface Contamination and Cleaning*, pp. 307–331, Elsevier, 2012.

[34] T. Fukuma, K. Kobayashi, K. Matsushige, and H. Yamada, "True molecular resolution in liquid by frequency-modulation atomic force microscopy," *Applied Physics Letters*, vol. 86, no. 19, p. 193108, 2005.

[35] S. Li, Y. Zhou, Y. Zi, G. Zhang, and Z. L. Wang, "Excluding contact electrification in surface potential measurement using kelvin probe force microscopy," *ACS nano*, vol. 10, no. 2, pp. 2528–2535, 2016.

[36] Y. Li, B. W. Maynor, and J. Liu, "Electrochemical afm "dip-pen" nanolithography," *Journal of the American Chemical Society*, vol. 123, no. 9, pp. 2105–2106, 2001.

[37] L. Kelvin, "V. contact electricity of metals," *The London, Edinburgh, and Dublin Philosophical Magazine and Journal of Science*, vol. 46, no. 278, pp. 82–120, 1898.

[38] I. Ovid'Ko, "Mechanical properties of graphene," *Rev. Adv. Mater. Sci*, vol. 34, no. 1, pp. 1–11, 2013.

[39] H.-J. Butt, B. Cappella, and M. Kappl, "Force measurements with the atomic force microscope: Technique, interpretation and applications," *Surface science reports*, vol. 59, no. 1-6, pp. 1–152, 2005.

[40] B. Cappella and G. Dietler, "Force-distance curves by atomic force microscopy," *Surface science reports*, vol. 34, no. 1-3, pp. 1–104, 1999.

[41] C. T. McKee, J. A. Last, P. Russell, and C. J. Murphy, "Indentation versus tensile measurements of young's modulus for soft biological tissues," *Tissue Engineering Part B: Reviews*, vol. 17, no. 3, pp. 155–164, 2011.

[42] T. G. Kuznetsova, M. N. Starodubtseva, N. I. Yegorenkov, S. A. Chizhik, and R. I. Zhdanov, "Atomic force microscopy probing of cell elasticity," *Micron*, vol. 38, no. 8, pp. 824–833, 2007.

[43] D.-M. Kaimaki, B. E. Smith, and C. Durkan, "On the use of nanomechanical atomic force microscopy to characterise oil-exposed surfaces," *RSC advances*, vol. 8, no. 12, pp. 6680–6689, 2018.

[44] C. Kittel, P. McEuen, and P. McEuen, *Introduction to solid state physics*, vol. 8. Wiley New York, 1996.

[45] J. Bardeen, "Theory of the work function. ii. the surface double layer," *Physical Review*, vol. 49, no. 9, p. 653, 1936.

[46] Y. Zhang, O. Pluchery, L. Caillard, A.-F. Lamic-Humblot, S. Casale, Y. J. Chabal, and M. Salmeron, "Sensing the charge state of single gold nanoparticles via work function measurements," *Nano Letters*, vol. 15, no. 1, pp. 51–55, 2014.

[47] M. Valden, X. Lai, and D. W. Goodman, "Onset of catalytic activity of gold clusters on titania with the appearance of nonmetallic properties," *science*, vol. 281, no. 5383, pp. 1647–1650, 1998.

[48] D. M. Wood, "Classical size dependence of the work function of small metallic spheres," *Physical Review Letters*, vol. 46, no. 11, p. 749, 1981.

[49] P. A. Anderson, "The contact difference of potential between tungsten and barium. the external work function of barium," *Physical Review*, vol. 47, no. 12, p. 958, 1935.

[50] J. T. Yates and L. G. Rubin, "Experimental innovations in surface science: A guide to practical laboratory methods and instruments," *Physics Today*, vol. 51, p. 66, 1998.

[51] H. L. Skriver and N. Rosengaard, "Ab initio work function of elemental metals," *Physical Review B*, vol. 45, no. 16, p. 9410, 1992.

[52] J. Weaver and D. W. Abraham, "High resolution atomic force microscopy potentiometry," *Journal of Vacuum Science & Technology B: Microelectronics and Nanometer Structures Processing, Measurement, and Phenomena*, vol. 9, no. 3, pp. 1559–1561, 1991.

[53] R. Schlaf, "Calibration of photoemission spectra and work function determination," 2014.

[54] K. P. F. Microscopy, "Measuring and compensating electrostatic forces," 2012.

[55] W. N. Hansen and G. J. Hansen, "Standard reference surfaces for work function measurements in air," *Surface science*, vol. 481, no. 1-3, pp. 172–184, 2001.

[56] A. S. Hyla, *Tailoring the work function of surfaces: Effects of charge transfer in surface modifiers on metals and transparent conducting oxides.* PhD thesis, Georgia Institute of Technology, 2016.

[57] W. Melitz, J. Shen, A. C. Kummel, and S. Lee, "Kelvin probe force microscopy and its application," *Surface science reports*, vol. 66, no. 1, pp. 1–27, 2011.

[58] M. Baghgar and M. D. Barnes, "Work function modification in p3ht h/j aggregate nanostructures revealed by kelvin probe force microscopy and photoluminescence imaging," *ACS nano*, vol. 9, no. 7, pp. 7105–7112, 2015.

[59] Y. Rosenwaks, R. Shikler, T. Glatzel, and S. Sadewasser, "Kelvin probe force microscopy of semiconductor surface defects," *Physical Review B*, vol. 70, no. 8, p. 085320, 2004.

[60] M. Nonnenmacher, M. o'Boyle, and H. K. Wickramasinghe, "Kelvin probe force microscopy," *Applied physics letters*, vol. 58, no. 25, pp. 2921–2923, 1991.

[61] J. Ren, H.-D. Ließ, R. Mäckel, and H. Baumgärtner, "Scanning kelvin microscope: a new method for surface investigations," *Fresenius' journal of analytical chemistry*, vol. 353, no. 3-4, pp. 303–306, 1995.

[62] J. Hsu, H. Ng, A. Sergent, and S. Chu, "Scanning kelvin force microscopy imaging of surface potential variations near threading dislocations in gan," *Applied Physics Letters*, vol. 81, no. 19, pp. 3579–3581, 2002.

[63] A. Kikukawa, S. Hosaka, and R. Imura, "Silicon pn junction imaging and characterizations using sensitivity enhanced kelvin probe force microscopy," *Applied Physics Letters*, vol. 66, no. 25, pp. 3510–3512, 1995.

[64] O. Vatel and M. Tanimoto, "Kelvin probe force microscopy for potential distribution measurement of semiconductor devices," *Journal of applied physics*, vol. 77, no. 6, pp. 2358–2362, 1995.

[65] K. Kaja, *Development of nano-probe techniques for work function assessment and application to materials for microelectronics.* PhD thesis, 2010.

[66] A. L. Domanski, E. Sengupta, K. Bley, M. B. Untch, S. A. Weber, K. Landfester, C. K. Weiss, H.-J. Butt, and R. Berger, “Kelvin probe force microscopy in nonpolar liquids,” *Langmuir*, vol. 28, no. 39, pp. 13892–13899, 2012.

[67] J. Sakai, M. Bavencoffe, B. Negulescu, P. Limelette, J. Wolfman, A. Tateyama, and H. Funakubo, “Strain-induced resistance change in v2o3 films on piezoelectric ceramic disks,” *Journal of Applied Physics*, vol. 125, no. 11, p. 115102, 2019.

[68] H. R. Rasouli, N. Mehmood, O. Çakıroğlu, E. C. Sürmeli, and T. S. Kasırga, “Synthesis of v 2 o 3 nanoplates for the exploration of the correlated supercritical state,” *Physical Review B*, vol. 100, no. 16, p. 161107, 2019.

[69] F. Morin, “Oxides which show a metal-to-insulator transition at the neel temperature,” *Physical review letters*, vol. 3, no. 1, p. 34, 1959.

[70] S. Shivashankar and J. Honig, “Metal—antiferromagnetic-insulator transition in v 2 o 3 alloys,” *Physical Review B*, vol. 28, no. 10, p. 5695, 1983.

[71] D. B. McWhan and J. P. Remeika, “Metal-insulator transition in $(V_{1-x}Cr_x)_2o_3$,” *Phys. Rev. B*, vol. 2, pp. 3734–3750, Nov 1970.

[72] S. Choi, Z. Shaolin, and W. Yang, “Layer-number-dependent work function of mos 2 nanoflakes,” *Journal of the Korean Physical Society*, vol. 64, no. 10, pp. 1550–1555, 2014.

[73] R. Wasilewski, “Elastic constants and youngs modulus of nial,” *AIME MET SOC TRANS*, vol. 236, no. 4, pp. 455–457, 1966.

[74] W. D. Callister, D. G. Rethwisch, *et al.*, *Materials science and engineering: an introduction*, vol. 7. John wiley & sons New York, 2007.

[75] S. Bertolazzi, J. Brivio, and A. Kis, “Stretching and breaking of ultrathin mos2,” *ACS nano*, vol. 5, no. 12, pp. 9703–9709, 2011.

[76] M. Remskar, “1.10 inorganic nanotubes beyond cylindrical matter,” *Comprehensive Nanoscience and Nanotechnology*, p. 237, 2019.

[77] J. A. Rogers, T. Someya, and Y. Huang, "Materials and mechanics for stretchable electronics," *science*, vol. 327, no. 5973, pp. 1603–1607, 2010.

[78] C. Chen, S. Rosenblatt, K. I. Bolotin, W. Kalb, P. Kim, I. Kymissis, H. L. Stormer, T. F. Heinz, and J. Hone, "Performance of monolayer graphene nanomechanical resonators with electrical readout," *Nature nanotechnology*, vol. 4, no. 12, p. 861, 2009.

[79] F. Liu, P. Ming, and J. Li, "Ab initio calculation of ideal strength and phonon instability of graphene under tension," *Physical Review B*, vol. 76, no. 6, p. 064120, 2007.

[80] K. He, C. Poole, K. F. Mak, and J. Shan, "Experimental demonstration of continuous electronic structure tuning via strain in atomically thin mos2," *Nano letters*, vol. 13, no. 6, pp. 2931–2936, 2013.

[81] D. Fotiadis, S. Scheuring, S. A. Müller, A. Engel, and D. J. Müller, "Imaging and manipulation of biological structures with the afm," *Micron*, vol. 33, no. 4, pp. 385–397, 2002.

[82] U. Komaragiri, M. Begley, and J. Simmonds, "The mechanical response of freestanding circular elastic films under point and pressure loads," *Journal of applied mechanics*, vol. 72, no. 2, pp. 203–212, 2005.

[83] L. Guo, H. Yan, Q. Moore, M. Buettner, J. Song, L. Li, P. T. Araujo, and H.-T. Wang, "Elastic properties of van der waals epitaxy grown bismuth telluride 2d nanosheets," *Nanoscale*, vol. 7, no. 28, pp. 11915–11921, 2015.

[84] J.-Y. Wang, Y. Li, Z.-Y. Zhan, T. Li, L. Zhen, and C.-Y. Xu, "Elastic properties of suspended black phosphorus nanosheets," *Applied Physics Letters*, vol. 108, no. 1, p. 013104, 2016.

[85] I. Frank, D. M. Tanenbaum, A. M. van der Zande, and P. L. McEuen, "Mechanical properties of suspended graphene sheets," *Journal of Vacuum Science & Technology B: Microelectronics and Nanometer Structures Processing, Measurement, and Phenomena*, vol. 25, no. 6, pp. 2558–2561, 2007.

[86] M. Poot and H. S. van der Zant, "Nanomechanical properties of few-layer graphene membranes," *Applied Physics Letters*, vol. 92, no. 6, p. 063111, 2008.

[87] D. A. Kunz, E. Max, R. Weinkamer, T. Lunkenbein, J. Breu, and A. Fery, "Deformation measurements on thin clay tactoids," *Small*, vol. 5, no. 16, pp. 1816–1820, 2009.

[88] B. Chitara and A. Ya'akobovitz, "Elastic properties and breaking strengths of gas, gase and gate nanosheets," *Nanoscale*, vol. 10, no. 27, pp. 13022–13027, 2018.

[89] R. C. Cooper, C. Lee, C. A. Marianetti, X. Wei, J. Hone, and J. W. Kysar, "Nonlinear elastic behavior of two-dimensional molybdenum disulfide," *Physical Review B*, vol. 87, no. 3, p. 035423, 2013.

[90] H. I. Rasool, C. Ophus, W. S. Klug, A. Zettl, and J. K. Gimzewski, "Measurement of the intrinsic strength of crystalline and polycrystalline graphene," *Nature communications*, vol. 4, no. 1, pp. 1–7, 2013.

[91] K.-T. Wan, S. Guo, and D. A. Dillard, "A theoretical and numerical study of a thin clamped circular film under an external load in the presence of a tensile residual stress," *Thin Solid Films*, vol. 425, no. 1-2, pp. 150–162, 2003.

[92] N. M. Bhatia and W. Nachbar, "Finite indentation of an elastic membrane by a spherical indenter," *International Journal of Non-Linear Mechanics*, vol. 3, no. 3, pp. 307–324, 1968.

[93] S. P. Timoshenko and S. Woinowsky-Krieger, *Theory of plates and shells*. McGraw-hill, 1959.

[94] C. Barth and C. R. Henry, "Kelvin probe force microscopy on mgo (001) surfaces and supported pd nanoclusters," *The Journal of Physical Chemistry C*, vol. 113, no. 1, pp. 247–253, 2008.

[95] G. López-Polín, C. Gómez-Navarro, V. Parente, F. Guinea, M. I. Katsnelson, F. Perez-Murano, and J. Gómez-Herrero, "Increasing the elastic modulus of graphene by controlled defect creation," *Nature Physics*, vol. 11, no. 1, pp. 26–31, 2015.

[96] D. Qiu, D. U. Lee, C. S. Park, K. S. Lee, and E. K. Kim, "Transport properties of unrestricted carriers in bridge-channel mos 2 field-effect transistors," *Nanoscale*, vol. 7, no. 41, pp. 17556–17562, 2015.

[97] S. Z. Butler, S. M. Hollen, L. Cao, Y. Cui, J. A. Gupta, H. R. Gutiérrez, T. F. Heinz, S. S. Hong, J. Huang, A. F. Ismach, *et al.*, "Progress, challenges, and opportunities in two-dimensional materials beyond graphene," *ACS nano*, vol. 7, no. 4, pp. 2898–2926, 2013.

[98] G. Eda, H. Yamaguchi, D. Voiry, T. Fujita, M. Chen, and M. Chhowalla, "Photoluminescence from chemically exfoliated mos2," *Nano letters*, vol. 11, no. 12, pp. 5111–5116, 2011.

[99] Z. Hu, T. Seeley, S. Kossek, and T. Thundat, "Calibration of optical cantilever deflection readers," *Review of Scientific Instruments*, vol. 75, no. 2, pp. 400–404, 2004.

[100] S. Hsieh, I.-T. Li, C.-W. Hsieh, M.-L. Kung, S.-L. Hsieh, D.-C. Wu, C.-H. Kuo, M.-H. Tai, H.-M. Wang, W.-J. Wu, *et al.*, "Advances in cellular nanoscale force detection and manipulation," *Arabian Journal of Chemistry*, 2015.

[101] J. E. Sader, J. W. Chon, and P. Mulvaney, "Calibration of rectangular atomic force microscope cantilevers," *Review of scientific instruments*, vol. 70, no. 10, pp. 3967–3969, 1999.

[102] Q. Yue, J. Kang, Z. Shao, X. Zhang, S. Chang, G. Wang, S. Qin, and J. Li, "Mechanical and electronic properties of monolayer mos2 under elastic strain," *Physics Letters A*, vol. 376, no. 12-13, pp. 1166–1170, 2012.

[103] P. Graves and D. Gardiner, "Practical raman spectroscopy," *Springer*, 1989.

[104] J. Shi, X. Wang, S. Zhang, L. Xiao, Y. Huan, Y. Gong, Z. Zhang, Y. Li, X. Zhou, M. Hong, *et al.*, "Two-dimensional metallic tantalum disulfide as a hydrogen evolution catalyst," *Nature communications*, vol. 8, no. 1, pp. 1–9, 2017.

[105] M. Hangyo, S.-I. Nakashima, and A. Mitsuishi, "Raman spectroscopic studies of mx2-type layered compounds," *Ferroelectrics*, vol. 52, no. 1, pp. 151–159, 1983.

[106] S. Nakashima, Y. Tokuda, A. Mitsuishi, R. Aoki, and Y. Hamaue, "Raman scattering from 2h-nbs2 and intercalated nbs2," *Solid State Communications*, vol. 42, no. 8, pp. 601–604, 1982.

[107] D. Eastman, "Photoelectric work functions of transition, rare-earth, and noble metals," *Physical Review B*, vol. 2, no. 1, p. 1, 1970.

[108] S. Hormeno, M. Penedo, C. V. Manzano, and M. Luna, "Gold nanoparticle coated silicon tips for kelvin probe force microscopy in air," *Nanotechnology*, vol. 24, no. 39, p. 395701, 2013.

[109] H. Sugimura, Y. Ishida, K. Hayashi, O. Takai, and N. Nakagiri, "Potential shielding by the surface water layer in kelvin probe force microscopy," *Applied physics letters*, vol. 80, no. 8, pp. 1459–1461, 2002.

[110] S. Sadewasser, T. Glatzel, R. Shikler, Y. Rosenwaks, and M. C. Lux-Steiner, "Resolution of kelvin probe force microscopy in ultrahigh vacuum: comparison of experiment and simulation," *Applied Surface Science*, vol. 210, no. 1-2, pp. 32–36, 2003.

[111] A. Lipatov, H. Lu, M. Alhabeb, B. Anasori, A. Gruverman, Y. Gogotsi, and A. Sinitskii, "Elastic properties of 2d ti3c2tx mxene monolayers and bilayers," *Science advances*, vol. 4, no. 6, p. eaat0491, 2018.

[112] I. Johnston, D. McCluskey, C. Tan, and M. Tracey, "Mechanical characterization of bulk sylgard 184 for microfluidics and microengineering," *Journal of Micromechanics and Microengineering*, vol. 24, no. 3, p. 035017, 2014.

[113] M. Annamalai, S. Mathew, M. Jamali, D. Zhan, and M. Palaniapan, "Effects of annealing on the ripple texture and mechanical properties of suspended bilayer graphene," *Journal of Physics D: Applied Physics*, vol. 46, no. 14, p. 145302, 2013.

[114] A. Falin, Q. Cai, E. J. Santos, D. Scullion, D. Qian, R. Zhang, Z. Yang, S. Huang, K. Watanabe, T. Taniguchi, *et al.*, "Mechanical properties of atomically thin boron nitride and the role of interlayer interactions," *Nature communications*, vol. 8, no. 1, pp. 1–9, 2017.

[115] J.-W. Jiang and Y.-P. Zhou, "Parameterization of stillinger-weber potential for two-dimensional atomic crystals," *arXiv preprint arXiv:1704.03147*, 2017.

[116] S. B. Desai, G. Seol, J. S. Kang, H. Fang, C. Battaglia, R. Kapadia, J. W. Ager, J. Guo, and A. Javey, "Strain-induced indirect to direct bandgap transition in multilayer wse2," *Nano letters*, vol. 14, no. 8, pp. 4592–4597, 2014.

[117] R. Fei and L. Yang, "Strain-engineering the anisotropic electrical conductance of few-layer black phosphorus," *Nano letters*, vol. 14, no. 5, pp. 2884–2889, 2014.

[118] S. Manzeli, A. Allain, A. Ghadimi, and A. Kis, "Piezoresistivity and strain-induced band gap tuning in atomically thin mos2," *Nano letters*, vol. 15, no. 8, pp. 5330–5335, 2015.